THE THREE GAP THEOREM IN PERSISTENT HOMOLOGY

By

Luis Suarez Salas

A DISSERTATION

Submitted to
Michigan State University
in partial fulfillment of the requirements
for the degree of

Applied Mathematics—Doctor of Philosophy
Computational Mathematics, Science, and Engineering—Dual Major

2024

ABSTRACT

The time delay (or Sliding Window) embedding is a technique from dynamical systems to reconstruct attractors from time series data. Recently, descriptors from Topological Data Analysis (TDA) — specifically, persistence diagrams — have been used to measure the shape of said attractors in applications including periodicity and quasiperiodicity quantification. Despite their utility, the fast computation of persistence diagrams of sliding windows embeddings is still poorly understood. In this work, we present theoretical and computational schemes to approximate the persistence diagrams of sliding window embeddings from quasiperiodic functions. We do so by combining the Three Gap Theorem from number theory with the Persistent Künneth formula from TDA, and derive fast and provably correct persistent homology approximations. The input to our procedure is the spectrum of the signal, and we provide numerical as well as theoretical evidence of its utility to capture the shape of toroidal attractors.

We begin our efforts by documenting the stability of using the Three Gap Theorem to compute persistence diagrams. The theorem relies on the continued fraction expansion of an irrational parameter. In turn, this expansion yields the k-th convergent which lie at the core of the result. This relation is leveraged to show that the number of matching continued fraction expansion terms on two parameter values can be used to bound the bottleneck distance of their corresponding persistence diagrams. This stability is then extended to the number of matching terms in their decimal expression. This is valuable since in practice we extract our parameters using the Fast Fourier Transform (FFT). Our results show exponential decay in bottleneck distance with respect to matching decimal terms. Ultimately, they validate the reliability of algorithms relying on continued fraction information, like our method 3G.

In the experiments presented here, our method took less than a second to run, on average. In linear computational time, it approximates persistence diagrams, which usually take exponential computational time. We demonstrated its performance by applying it to dynamical systems from a wide range of scientific disciplines. We are able to successfully approximate persistence diagrams within known error bounds and our work contributes to the implementation of TDA on larger data

sets.

TABLE OF CONTENTS

CHAPTER 1

INTRODUCTION

Scientific observation is at the heart of models and theories. Measurements obtained from the real world guide and validate a framework. For instance, in neuroscience, the Wilson-Cowan equations were able to recreate oscillatory behavior that had been independently observed in spiking activities of motor neurons [1]. The model consists of two driving forces: excitatory and inhibitory neurons, depicted in Figure 1.1. The spiking of these two types of neurons can be directly measured in the

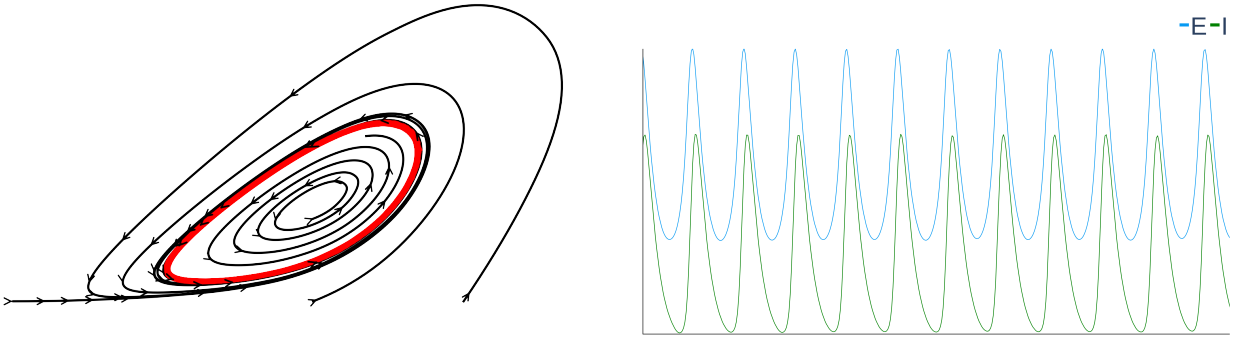

Figure 1.1 We illustrate the oscillatory behavior the Wilson-Cowan equations can replicate. On the left, we plot different trajectories in the IE-plane. On the right, we plot the solution corresponding to the red trajectory.

real world. This generates a time series which is a measurement of a variable across time. A time series is capable of capturing critical information that is difficult to retrieve. How much information can it contain? A task not worth considering, being ill-posed, is aiming to use observed spiking activities of motor neurons to infer the number of neurons and their size. Rather, reconstructing qualitative information is within reach. This type of information is what the model aimed for in the first place as it is better suited for the study of higher functions in the brain: The number of neurons discards the possibility of measuring them individually, pattern recognition is a global process, and there is an abundance of local randomness that gains precision on long-range interactions [1]. Other fields of science care about qualitative information for analogues reasons. Hence, it is imperative to be able to determine qualitative information of a system using a time series as input. Topological data analysis (TDA) offers a framework to achieve this that can be applied across

different fields of science. However, a current limitation is the computational complexity it takes. This motivated our work which provides a much more feasible alternative. It relies on computing an approximation leveraging results in Fourier analysis and number theory. Ultimately, we hope to alleviate computational constraints, and in turn facilitate implementation to a wider class of data sets.

Mathematically, we denote a time series as $f : \mathbb{R} \to \mathbb{C}$. Conceptually, we think of it as the information obtained from measuring a mechanism that changes over time. The spiking of excitatory and inhibitory neurons, $E(t)$ and $I(t)$, respectively, are examples of time series data. They provide a glimpse into a more complex structure: the nervous system. This is an example of a dynamical system, which pertains to a theory fit to model non-linear processes. A dynamical system is composed of [2]:

1- A phase space, which consists of all the possible states of the system. This takes the form of an N-dimensional manifold M.

2- The dynamical part which captures how the system changes across time. This is a continuous map $\Phi : \mathbb{R} \times M \to M$ such that $\Phi(0, p) = p$ and $\Phi(s, \Phi(t, p)) = \Phi(s + t, p)$ for $p \in M$ and $t, s \in \mathbb{R}$.

A dynamical system, like the ones shown in Figure 1.2, can be obtained from a set of differential

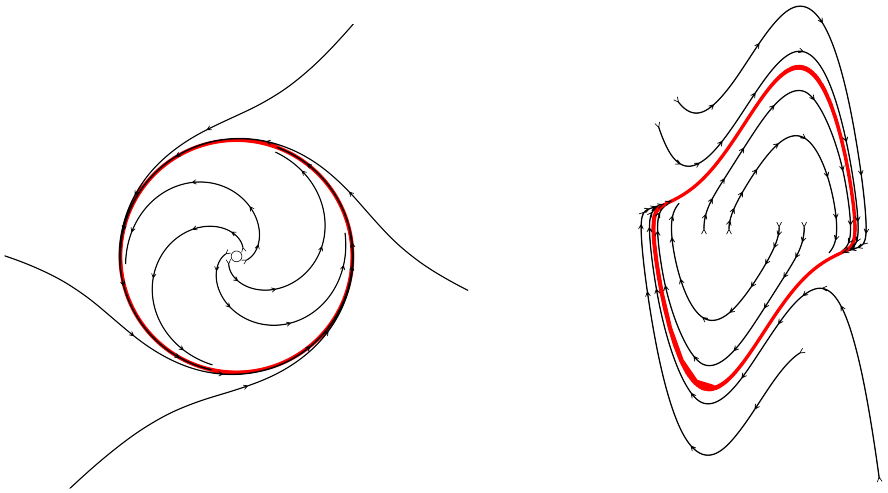

Figure 1.2 We illustrate two dynamical systems. By looking at their phase space, without the need of any coordinate axis information, we can conclude they exhibit periodicity. Indeed, the convergence of trajectories to the red trajectory indicates the presence of a toroidal attractor.

equations like the Wilson-Cowan equations. The equations represent the constraints of the system. For example in physics, they could be the ones governing the motion of an object. In neuroscience, they could be the ones describing the action potential interaction of neurons. The end result is the evolution of a system across time described entirely by equations. Nevertheless, for many dynamical systems of interest, the governing equations are unknown. All that can be extracted are measurements of the system. This leads to the task of reconstructing the underlying dynamical system using time series data. The endeavour of reconstructing an unknown dynamical system using observational data has been treated by Takens' Theorem [3]. It allows for the use of signals such as $E(t)$ or $I(t)$ to recover behavior in phase space such as the red trajectories shown in Figure 1.1 and 1.2. Concretely, it demonstrates that almost any observation from an unknown dynamical

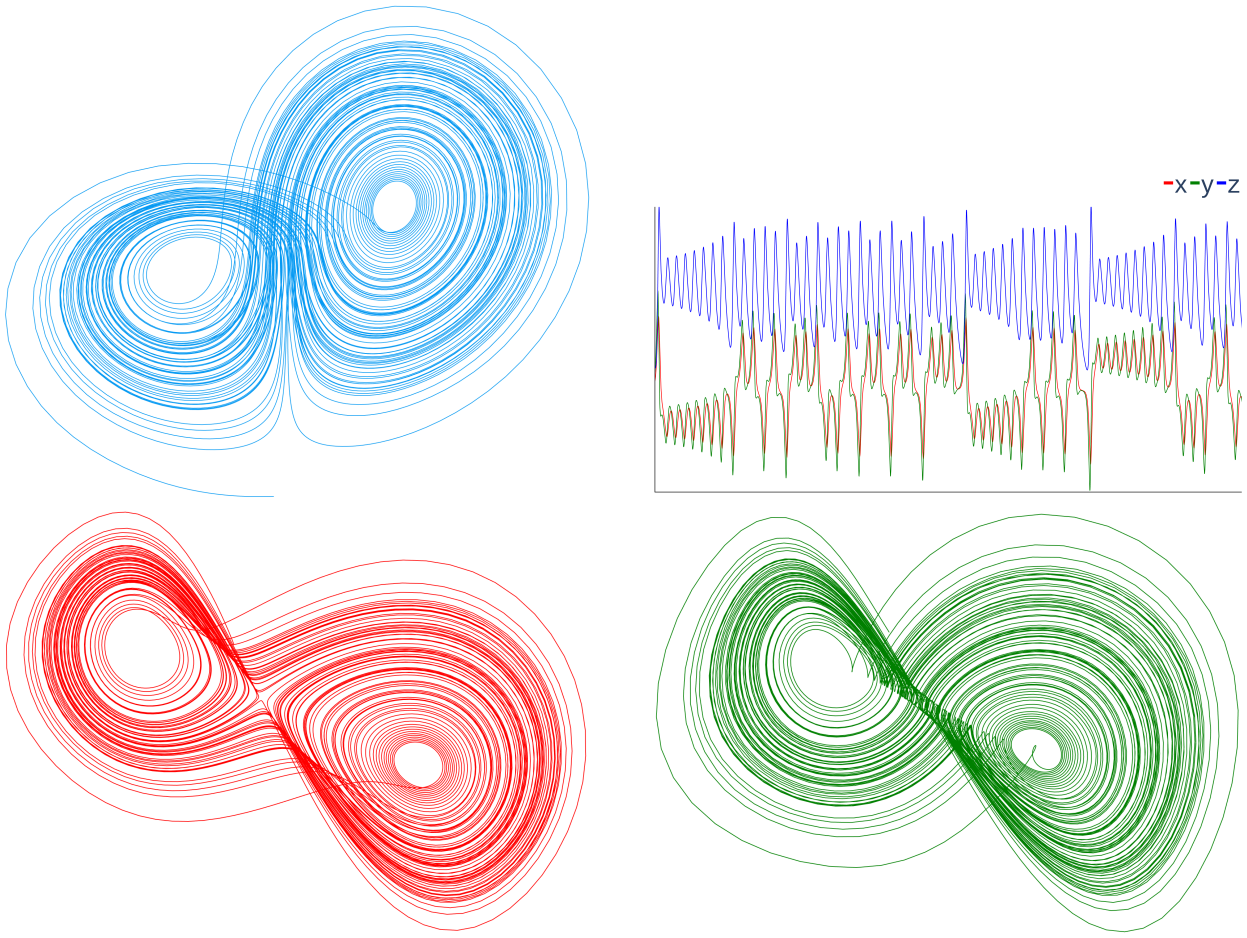

Figure 1.3 Top row: On the left we plot the butterfly wings generated by the Lorenz system. On the right we show a solution of the system. Bottom row: We can reconstruct the Lorenz attractor $x(t)$, shown on the left, and $y(t)$, shown on the right, thanks to Takens' Theorem.

system can be used to recover important information from the system: the topology of attractors. In other words, we start with an unknown topological metric space, sampled by a trajectory in the phase space pf the dynamical system, and are able to reconstruct a topologically equivalent copy in Euclidean Space, like shown in Figure 1.3. This is of great significance as the shape traced in the phase space provides qualitative information of the system [4]. In particular, it can indicate the presence of recurrent behavior such as periodicity or quasiperiodicity [4, 5, 6, 7]. Indeed, as shown in Figure 1.1, the red trajectory corresponds to oscillations of $E(t)$ and $I(t)$.

Quasiperiodicity is a repetitive behavior generalizing the notion of periodicity, see Figure 1.4. It does so by incorporating at least two $\mathbb{Q}$-linearly independent frequencies, i.e. incommensurate. This type of signal is amply documented in the scientific literature. It has been observed in crystal formations, studies of mammal vocalizations, fMRI scans obtained from mice, and electrocardiograms [8, 9, 10, 11]. The list goes on. Furthermore, it is known to be an intermediary state between chaos and stability [12, 13]. Thus, its presence is of great interest across scientific fields. Fortunately, we are able to better understand this behavior using tools from topological data analysis. Indeed, persistence diagrams have been successfully used to detect the presence of quasiperiodicity in signals [5, 6, 7].

The method used to detect quasiperiodic signals, depicted in Figure 1.4, is the Sliding Window Embedding Technique (SW). This takes a time series f and creates an embedding

$$SW_{d,\tau} f(t) = \begin{bmatrix} f(t) \\ f(t+\tau) \\ \vdots \\ f(t+d\tau) \end{bmatrix} \in \mathbb{C}^{d+1}.$$

By Takens' Theorem, this map can preserve the topology of attractors of the original dynamical space. Furthermore, it has been shown that the embedding will be dense in a space homeomorphic to an N-dimensional torus if and only if f is a quasiperiodic signal with N incommensurate frequencies [5]. Thus, quasiperiodicity detection reduces to showing that the shape of the reconstruction is topologically an N-dimensional torus. This is an ideal task for persistent homology as it creates

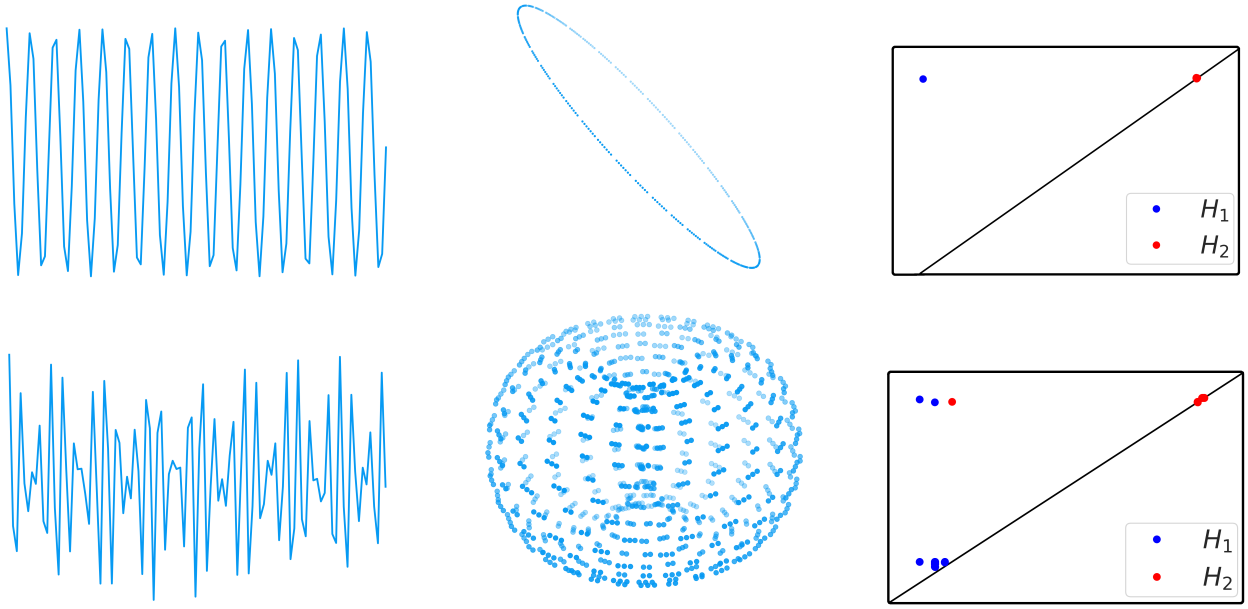

Figure 1.4 The SW starts with a signal, followed by a reconstruction of the phase space, and concludes with the computation of persistent homology. Top row: SW done with a periodic signal. Bottom row: SW done with a quasiperiodic signal generated by two incommensurate frequencies.

an abstract simplicial complex from a discrete set of points. It then computes the homology of the complex across a distance parameter. This provides a robust way of estimating the underlying topology of a set of points. For our purposes, we look for the characterizing homology of the N-torus. In the periodic case, such as the Wilson-Cowan dynamical system and the ones shown in Figure 1.2, we have the topology of a 1-dimensional torus, namely a circle.

Much work has been done proving the usefulness of SW [6, 7, 14]. Furthermore, there is a well defined way of optimizing the embedding parameters d and τ [5]. A current limitation is the time it takes to compute persistent homology. The first persistence algorithm is of the order $O(n^3)$ where n is the number of simplices [15]. In practice, one uses Ripser [16], which improves running time but is still exponential [17]. This proves to be computationally taxing for most data sets, and motivated our project of creating an approximation method that would provide a much faster and computationally accessible alternative.

Our method relies on The Three Gap Theorem which in turn benefits from the theory of

continued fractions. The latter studies the expansion of an irrational number, say ω, of the form

$$\omega = a_1 + \cfrac{1}{a_2 + \cfrac{1}{a_3 + \cfrac{1}{a_4 + \cdots}}} := [a_1, a_2, a_3, \cdots],$$

where $a_1 \in \mathbb{Z}$ and $a_i \in \mathbb{N}$. There are infinite non-zero terms a_i when ω is irrational [18]. Furthermore, these terms capture important information. Indeed, consider the continued fraction expansion of the golden ratio:

$$\varphi = 1 + \cfrac{1}{1 + \cfrac{1}{1 + \cfrac{1}{1 + \cdots}}}.$$

One can readily use this expression to argue φ is the most irrational number. There is much more than can be said by looking at continued fraction expansions. Their connection with geometry is deeply rooted [19].

We leverage continued fractions to better understand the distribution of points in the set

$$S_{\omega,T} := \{[i\omega]\}_{i=0}^{T},$$

where $[x] = x \bmod 1$. By the Three Gap Theorem, the distance between adjacent points in this set can take at most three different values [20]. Remarkably, this result is independent of ω and T.

By identifying the endpoints of $[0, 1]$, we can think of $S_{\omega,T}$ as a sampling of the circle. Thus, knowing the gaps in this set can directly transfer to knowing its 0-th dimensional persistence homology as depicted in Figure 1.5. We then make the jump to the N-torus by taking a Cartesian product of the form

$$\prod_{i=0}^{N} S_{\omega_i,T}.$$

We can also compute persistence homology in this case thanks to the Künneth Formula in persistence homology [14]. For the study of quasiperiodicity, this provides us with an alternative to using Ripser to compute persistence diagrams. Indeed, we can use the fast fourier transform of time series data to estimate the incommensurate frequencies. That this will work for general quasiperiodic signals is thanks to the results in [5]. We are thus in a position to leverage frequency information thanks to The Three Gap Theorem. This makes it possible to compute an approximation that includes error bounds without the use of Ripser at any step, resulting in linear time complexity, see Figure 4.5.

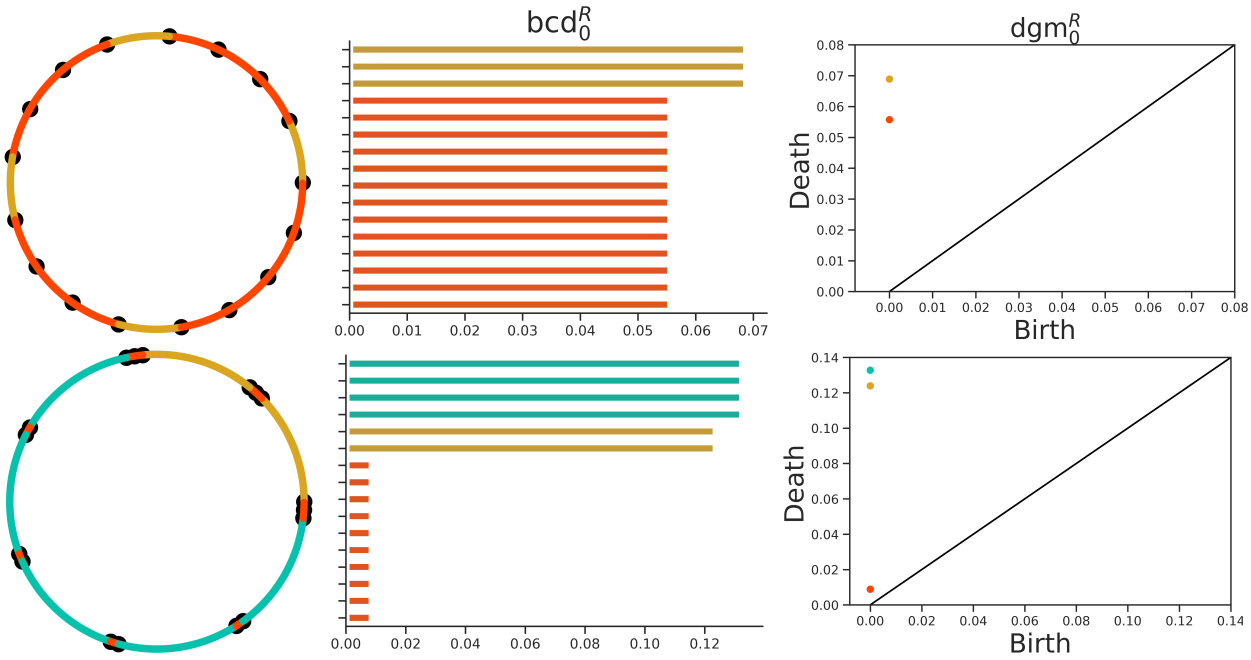

Figure 1.5 We illustrate the result of the three gap theorem and how they translates directly to results in persistence homology. Left column: Depiction of the sets $S_{\pi-1,17}$ (top) and $S_{\sqrt{5},17}$ (bottom). Middle column: Corresponding persistence barcodes. Right column: Corresponding persistence diagrams. We note $d_2(\pi - 1, \sqrt{5}) = 0.094$.

1.1 Outline and Overview

We move on to detailing the structure of this dissertation. The next section will cover background definitions followed by our stability results for the use of The Three Gap Theorem in persistence computations, then we will present our approximation method, 3G, and we will conclude with applications of it to the study of dynamical systems.

1.1.1 Background

Persistent homology is the main tool used for our work. Thus, we begin by presenting a complete treatment of definitions and concepts. We also include important theorems and results we use in our method. Ultimately, persistent homology is intended to investigate reconstructed dynamical systems. This leads to the Sliding Window Embedding, which is how we take a time series and create a point cloud in a higher dimension. We then compute its persistence homology to analyze its shape. This is followed by a brief subsection on Fourier series, in particular we present the multidimensional case and relate it to persistence diagrams. We then introduce the theory of

continued fraction expansions. This leads naturally to The Three Gap Theorem. We end with a schematic of our method.

1.1.2 Stability of The Three Gap Theorem in Persistence Diagrams

Our work begins by presenting theoretical justifications for the use of The Three Gap Theorem in persistence homology. We do so by looking at the stability of the bottleneck distance of the corresponding persistence diagrams from sampling parameters. Our work shows conditions that justify the use of continued fraction expansion of decimals obtained from numerical approximations. In particular, we show that for two parameters with the same first j decimals:

Proposition 3.2.8 *Suppose ω and $\bar{\omega}$ are two irrational numbers having the same first j decimals, denoted as*

$$x_j = \bar{x}_j,$$

for some $j \in \mathbb{N}$. If $0 < T < q_{k_j(\omega)-1}$, where $q_n(\omega)$ denotes the n-th convergent of ω, then for $i \geq 0$ the bottleneck distance d_B is bounded by

$$d_B(dgm_i^R(S_{\omega,T}), dgm_i^R(S_{\bar{\omega},T})) \leq \frac{1}{q_{k_j(\omega)}}.$$

Furthermore, we can show the error decays exponentially in probability

Theorem 3.2.10 *For $0 < \epsilon < z_0$ there exists positive constants C, λ (depending on ϵ) with $0 < \lambda < 1$ such that for all integers $j \geq 1$ for which*

$$x_j = \bar{x}_j,$$

and $T < q_{k_j(\omega)-1}$, if $k_j(\omega) \geq jz_0$, then for $i \geq 0$

$$P\left(d_B(dgm_i^R(S_{\omega,T}), dgm_i^R(S_{\bar{\omega},T})) \leq \frac{1}{j(\epsilon + z_0)}\right) \leq C\lambda^j,$$

otherwise

$$P\left(d_B(dgm_i^R(S_{\omega,T}), dgm_i^R(S_{\bar{\omega},T})) \leq \frac{1}{j(z_0 - \epsilon)}\right) \geq 1 - C\lambda^j.$$

These results are corroborated by our applications at the end of the section. They illustrate numerical stability that carries over to our approximation method based on The Three Gap Theorem.

1.1.3 Estimation of Persistence Diagrams Via The Three Gap Theorem

In this section we present our approximation method 3G. It is based on theoretical guarantees of The Three Gap Theorem described above and the Künneth formula in persistence homology. Specifically, we are able to take a quasiperiodic signal and perform computations using each incommensurate frequency in parallel. We then put everything together to obtain an approximation to the persistence diagram of the Sliding Window point cloud of interest. We obtain error bounds with our approximation and demonstrate it computes much faster. An outline of our contribution is as follows:

1. Start with an observation signal f.

2. Reconstruct the phase space by computing $\{SW_{d,\tau}f(t)\}_{t=0}^{T}$.

~~3.~~ Compute $\mathrm{dgm}_j^R(\{SW_{d,\tau}f(t)\}_{t=0}^{T}, d_2)$ using **Ripser**.

3. (a) Use the FFT to retrieve the frequencies of f and then use them to compute continued fraction expansions.

(b) Use them as shown in Section 4.2 and then apply the results from Section 4.3 to approximate $\mathrm{dgm}_j^R(\{SW_{d,\tau}f(t)\}_{t=0}^{T}, d_2)$.

Figure 1.6 Steps involved in SW. Our method provides an alternative to number 3.

1.1.4 Applications

We conclude by considering different quasiperiodic dynamical systems. Using the SW we are able to verify this behavior. We then apply our 3G method to approximate the persistence diagrams obtained from SW. We show our method computes much faster and plot the resulting persistence diagrams with their corresponding error bounds. Shown below is the result obtained when considering the pendulum attached to a sliding block. Understanding this system translates to improvement in earthquake damping technology for skyscrapers [21, 22].

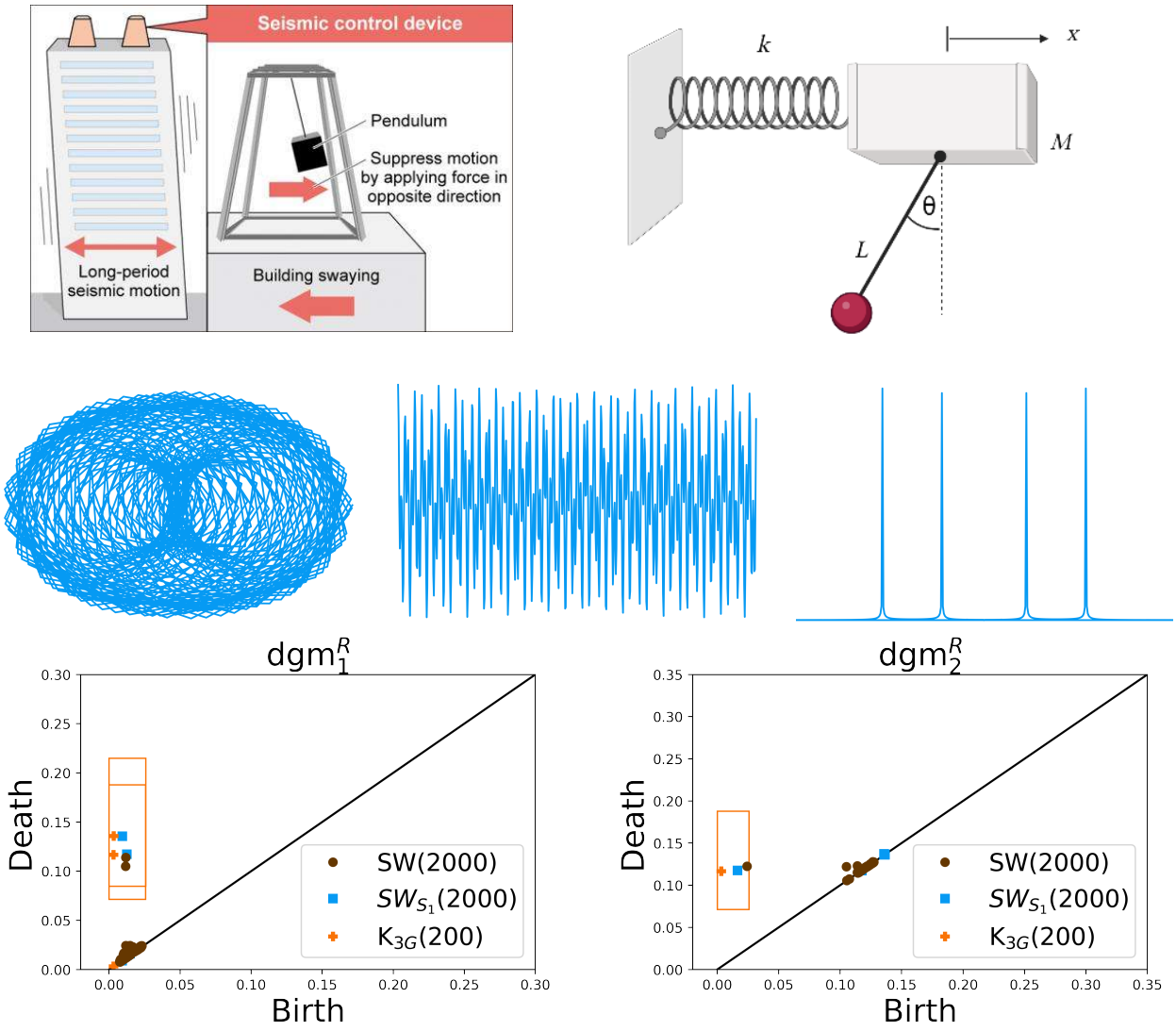

Figure 1.7 Top row: Depiction of anti-earthquake technology taken from [23]. The system on the right models the dynamics of this technology. Middle row: Plot of $(x, \dot{x})$ from the pendulum attached to a sliding block. The solution $x(t)$ we used for SW is plotted in the middle followed by the modulus of its Fast Fourier Transform. Bottom row: Persistence diagrams showing our proposed approximation K_{3G}. The rectangle depicts the theoretical approximation bound.

CHAPTER 2

BACKGROUND

In this section we cover results and definitions needed to present our results. For the most part, our work pertains to persistent homology. Moreover, our contribution involves theoretical guarantees from number theory and Fourier analysis. We thus attempt to present these separate elements in a concise but complete fashion. We begin by thoroughly defining persistent homology and the important results we rely on. This is followed by a definition of dynamical systems. Our main aim in this section is to highlight the reconstruction theorem of Takens and its connection to the Sliding Window Embedding technique (SW). We then move to recall the Fourier transform and detail its connection to SW. This is followed by the presentation of continued fraction expansions and their properties. This will naturally lead to The Three Gap Theorem, the pillar of our work. We conclude with a schematic of our method 3G that highlights the integration of the different components involved.

2.1 Persistent Homology

This section covers the abstract notion of shape we can assign to discrete data. We begin by presenting the main object to which we can assign a shape to. Most definitions were taken from [24, 5].

Definition 2.1.1. *Given a set X, an abstract simplicial complex K with vertices in X, is a collection of subsets of P(X) such that*

1. *Every $\sigma \in K$ is finite,*
2. *For any $\sigma \in K$, if $\tau \neq \varnothing$ and $\tau \subset \sigma$ then $\tau \in K$.*

The sets in K are called simplices and the dimension of a simplex is defined as $\dim(\sigma) = |\sigma| - 1$. We also define $\dim(K) = \max\{\dim(\sigma)\}$. A face of σ is any non empty proper set of it. The n-th skeleton of K is denoted by $K^{(n)} := \{\sigma \in K : \dim(\sigma) \leq n\}$. In particular, $K^{(0)}$ is called the set of vertices of K and $K^{(1)}/K^{(0)}$ is called the set of edges of K. A subcomplex L of K, which we denote $L \subset K$, is an abstract simplicial complex for which $L^{(n)} \subset K^{(n)}$ for all $n \in \mathbb{Z}$.

Example 2.1.2. *Let X be a finite set. One can readily check that the power set, $P(X)$, generates an abstract simplicial complex.*

Example 2.1.3. *Any partially ordered set X can form an abstract simplical complex. Indeed, the faces can be defined as the totally ordered subsets of X. This abstract simplicial complex is known as the order complex of X.*

We can construct an abstract simplicial complex from any discrete set of points in a metric space. Indeed, this is achieved by constructing the Rips complex which treats each data point in a metric space, say $x_i \in (X, d)$, as a vertex. Edges $\{x_0, x_1\}$ are created between two vertices if their distance is less than some fixed $\epsilon > 0$, i.e. $d(x_0, x_1) < \epsilon$. Connecting three vertices creates a triangle $\{x_0, x_1, x_2\}$, four a tetrahedron $\{x_0, x_1, x_2, x_3\}$, and so on. Once can think of the result as a triangulated space.

Definition 2.1.4. *Given a finite metric space (X,d) and a real number $\epsilon > 0$ we define the Rips complex $R_\epsilon(X, d)$ to be the simplicial complex defined as*

$$\left\{ \{x_0, \ldots, x_n\} \subset X |\ d(x_i, x_j) < \epsilon \ \forall_{0 \le i,j \le n} \right\}.$$

With this construction we can begin using a powerful shape descriptor: homology. This tool assigns a topological invariant to an abstract simplicial complex. For instance, the 0-th dimensional homology corresponds to connected components. The 1-st dimensional homology detects loops and the 2-nd dimensional homology closed surfaces that are hollow. In general the n-th dimensional homology detects n-dimensional holes. We first present the algebraic structures required.

Let K be a simplicial complex and G and abelian group.

Definition 2.1.5. *The n-th chain group $C_n(K; G)$ of K with coefficients in G is*

$$C_n(K; G) := \left\{ \sum_{i \in I} g_i \sigma_i : \sigma_i \in K^{(n)} \setminus K^{(n-1)},\ g_i \in G \text{ and } g_i \neq 0 \text{ for only finitely many } i \in I \right\}.$$

We refer to a $\tau \in C_n(K; G)$ as a n-chain.

Definition 2.1.6. *The n-th boundary map* $\partial_n : C_n(K;G) \longrightarrow C_{n-1}(K;G)$ *is a group homomorphism defined for any* $\sigma = [v_0, \ldots, v_n] \in K^{(n)}/K^{(n)-1}$ *as*

$$\partial_n(\sigma) = \sum_{i=0}^{n} (-1)^n [v_0, \ldots, \hat{v_i}, \ldots, v_n]$$

where $[v_0, \ldots, \hat{v_i}, \ldots, v_n]$ *denotes the* $(n-1)$*-th face of* σ *obtained from deleting the vertex* v_i *from the set* $\{v_0, \ldots, v_n\}$.

Definition 2.1.7. *A chain complex is a collection of* $C_* = \{C_i, f_i\}_i$ *of groups* C_i *and morphisms* $f_i : C_i \longrightarrow C_{i-1}$ *such that* $f_{i-1} f_i = 0$.

Definition 2.1.8. *The i-th homology group of a chain complex* C_* *with coefficients in a group G is defined as*

$$H_i(C_*;G) := \frac{ker(f_i)}{img(f_{i+1})}.$$

Our work restricts to the chain complex $C_* = \{C_i(K;G), \partial_i\}_{i \in \mathbb{N}}$, thus we adopt the notation $H_i(K;G)$. Furthermore, our abstract simplicial complex is obtained from the Rips complex of discrete data in a metric space (X,d), i.e. $K = R_\epsilon(X,d)$ and we work with coefficient in a field, i.e. $G = \mathbb{F}$. We denote the resulting i-th homology in this case as $H_i(R_\epsilon(X,d);\mathbb{F})$. We note the result is a vector space whose basis elements represent i-th dimensional holes in the Rips complex $R_\epsilon(X,d)$.

Persistent homology is obtained from the computation of homology for all $\epsilon \in [0,\infty)$. Since $R_\epsilon(X,d) \subset R_{\epsilon'}(X,d)$ for $\epsilon \leq \epsilon'$, we can obtain linear maps

$$T_{\epsilon,\epsilon'} : H_i(R_\epsilon(X,d);\mathbb{F}) \longrightarrow H_i(R_{\epsilon'}(X,d);\mathbb{F})$$

between vector spaces. Thus, we can keep track of the number of i-th dimensional holes as ϵ changes. This corresponds to changes in the topology of the Rips complex. For example, three connected components can become one, or a hollow closed surface can be filled. We detail this notion.

Definition 2.1.9. *A filtered complex $\mathcal{K}$ is a collection of simplicial complex $\{K_\epsilon\}_{\epsilon \geq 0}$ such that*

$$K_\epsilon \subset K_{\epsilon'}$$

when $\epsilon \leq \epsilon'$.

We refer to $\mathcal{K}$ as a filtration.

Definition 2.1.10. *Let*

$$H_i(\mathcal{K}; \mathbb{F}) = \left\{ T_{\epsilon,\epsilon'} : H_i(K_\epsilon; \mathbb{F}) \longrightarrow H_i(K_{\epsilon'}; \mathbb{F}),\ \epsilon \leq \epsilon' \right\}$$

denote the family of $\mathbb{F}$-vector spaces and linear transformations $T_{\epsilon,\epsilon'}$ induced by the inclusion maps $K_\epsilon \hookrightarrow K_{\epsilon'}$, for $\epsilon \leq \epsilon'$. The i-th persistent homology groups are

$$H_i^{\epsilon,\epsilon'}(\mathcal{K}; \mathbb{F}) := Img(T_{\epsilon,\epsilon'})$$

and their dimension over $\mathbb{F}$ are the persistent Betti numbers

$$\beta_i^{\epsilon,\epsilon'}(\mathcal{K}) := rank(T_{\epsilon,\epsilon'}) = dim_{\mathbb{F}}\big(H_i^{\epsilon,\epsilon'}(\mathcal{K}; \mathbb{F})\big).$$

For our purposes, $H_i(\mathcal{K}; \mathbb{F})$ will satisfy the pointwise-finite condition, i.e. $\beta_i^{\epsilon,\epsilon}(\mathcal{K}) < \infty$ for every ϵ. This will imply that the isomorphism type of $H_i(\mathcal{K}; \mathbb{F})$ is uniquely determined by a multiset of intervals $I \subset [0, \infty]$ [25]. These intervals are called the barcode of $H_i(\mathcal{K}; \mathbb{F})$ and are denoted $\text{bcd}_i(\mathcal{K})$. We use the notation $\text{bcd}_i^R(X, d)$ to highlight we are working with the Rips complex of a metric space. A bar in the barcode, with endpoints $a, b \in \mathbb{R}_{\geq 0}$ and $a < b$, indicates when a i-th dimensional hole first appears and disappears. Indeed, it represents a new basis element at $\epsilon = a$ (birth) and that this basis element will persist until it is lost at $\epsilon = b$ (death). We refer to $b - a$ as the lifetime of a basis element.

Plotting $\text{bcd}_i^R(X, d)$ in the plane, now as $(a, b) \in \mathbb{R}^2$, gives the persistence diagram. On it, points that are far away from the line $y = x$ represent topological features in data that are more reliable. Namely, the ones having longer lifetime. We denote them analogously as $\text{dgm}_i^R(X, d)$.

The space of persistence diagrams can be given a metric, the bottleneck distance d_B [26]. In the following definition we consider the points in the diagonal $y = x$ as part of the persistence diagram.

Definition 2.1.11. *Let $\mathcal{K}_1$ and $\mathcal{K}_2$ be two filtrations. We define the bottleneck distance between their i-th persistence diagram as*

$$d_B(dgm_i(\mathcal{K}_1), dgm_i(\mathcal{K}_2)) = \inf_{\phi: dgm_i(\mathcal{K}_1) \to dgm_i(\mathcal{K}_2)} \{ \sup_{y \in dgm_i(\mathcal{K}_1)} \{\|y - \phi(y)\|_\infty\}\},$$

where ϕ is a bijection of multisets.

Conceptually, given two persistence diagrams we consider a map that pairs points between them. This forms a pairing to which we can assign a value using the infinity norm of each pair. We then look at all the combinations of pairings and find the smallest value possible. In essence, this captures how similar two persistence diagrams are to each other in the plane. We note that including the infinite points on the diagonal in each persistence diagram allows for a pairing every time.

When working with metric spaces, we can connect the bottleneck distance with the Gromov-Hausdorff distance. The latter measures the similarity between bounded metric spaces [5].

Definition 2.1.12. *Given two non-empty subsets A and B of a metric space (X, d), the* Hausdorff distance $d_H(A, B)$ *is defined as:*

$$d_H(A, B) = \max \left\{ \sup_{a \in A} \inf_{b \in B} d(a, b), \sup_{b \in B} \inf_{a \in A} d(b, a) \right\},$$

where $d(a, b)$ denotes the distance between points a and b in X.

Definition 2.1.13. *For two metric spaces (X_1, d_1) and (X_2, d_2), the Gromov-Hausdorff distance $d_{GH}(X_1, X_2)$ is defined as the infimum of the Hausdorff distances between the images of X_1 and X_2 in any common metric space Z, over all isometric embeddings $\phi_1 : X_1 \to Z$ and $\phi_2 : X_2 \to Z$:*

$$d_{GH}(X_1, X_2) = \inf_{Z, \phi_1, \phi_2} d_H(\phi_1(X_1), \phi_2(X_2)).$$

The connection is illustrated in the following result.

Theorem 2.1.14. *Let X_1 and X_2 be totally bounded metric spaces. Then*

$$d_B(bcd_i^R(X_1, d), bcd_i^R(X_2, d)) \leq 2 d_{GH}(X_1, X_2).$$

We conclude this section by presenting a result that applies to the barcodes of a cross product space.

Definition 2.1.15. *Let (X, d_X) and (Y, d_Y) be metric spaces. The maximum metric d_M is given by*

$$d_M\big((x, y), (x', y')\big) := \max\{d_X(x, x'), d_Y(y, y')\},$$

where $(x, y), (x', y') \in X \times Y$.

We note $(X \times Y, d_M)$ is a metric space. Furthermore, its barcodes are given by [14]:

Theorem 2.1.16 (Persistent Künneth Formula). *Let (X, d_X) and (Y, d_Y) be metric spaces. Then,*

$$bcd_n^R(X \times Y, d_M) = \bigcup_{i+j=n} \big\{I \cap J \mid I \in bcd_i^R(X, d_X),\ J \in bcd_j^R(Y, d_Y)\big\},$$

for all $n \in \mathbb{N}$.

2.2 Dynamical Systems

Now that we presented persistent homology as the tool that allow us to assign shape to discrete data, we now present the framework that models the source of data. Indeed, real world scientific observations depict an underlying mechanism. Although this mechanism may be unknown to us or of immense complexity, the theory of dynamical systems enable us to describe it mathematically. The framework consists of a phase space M that represents all of the relevant states of the system and a function Φ that keeps track of the evolution of the system. Definitions were taken from [2].

Definition 2.2.1. *A global continuous time dynamical system is a pair (M, Φ), where M is a topological space and $\Phi : \mathbb{R} \times M \longrightarrow M$ is a continuous map so that $\Phi(0, p) = p$, and $\Phi(s, \Phi(t, p)) = \Phi(s + t, p)$ for all $p \in M$ and all $t, s \in \mathbb{R}$.*

We note that a system of ordinary differential equations can give rise to a dynamical system in which M is a smooth manifold. In this case, the dynamics Φ are given by the integral curves obtained from the system of equations. One can then see that systems modeled by differential equations are dynamical systems. The evolution of the system is completely determined by the constrains captured by the equations and the starting state, i.e. the initial condition.

Example 2.2.2. *Consider the motion of a pendulum without damping or external driving forces. In this case, the equation governing motion is given by*

$$\frac{d^2\theta}{d^2t} + \frac{g}{L}\sin(\theta) = 0,$$

where θ is the angle made from the downward vertical, g is the acceleration due to gravity, and L is the length of the pendulum. One can show the phase space M is two dimensional depending only on θ and $\dot{\theta}$. This means that if we known their value at any point in time, we can then fully describe the evolution of the system. We illustrate different trajectories in the $\theta\dot{\theta}$-plane representing the dynamics obtained when placing the hanging mass θ_o from the vertical and then letting it fall, see Figure 2.1.

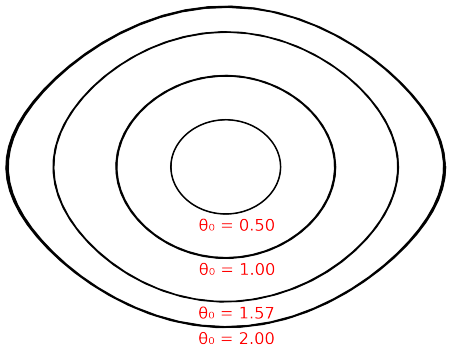

Figure 2.1 The phase space of the simple pendulum lies in the $\theta\dot{\theta}$-plane (Example 2.2.2). We illustrate different trajectories with initial condition $(\theta_o, 0)$. The motion is well known to be periodic, this is captured by the shape of circular trajectories in M.

Example 2.2.3. *The Wilson-Cowan equations were introduced in 1972 [1]. They have found great success accounting for behavior observed in neurons [27, 28]. The phase space M is two dimensional. It lies in the IE-plane, where I corresponds to spiking inhibitory neurons and E for spiking excitatory neurons. The equations involve a sigmoid function $\mathcal{S}$, we present the one in [1], However, as noted in their work, any sigmoid function is valid.*

$$\tau_1\frac{dE}{dt} = -E + (k_1 - r_1E)\mathcal{S}_1(c_1E - c_2I + P(t)),$$

$$\tau_2 \frac{dI}{dt} = -I + (k_2 - r_2 I)\mathcal{S}_2(c_3 E - c_4 I + Q(t)),$$

where

$$\mathcal{S}_i(x) = \frac{1}{1 + e^{-a_i(x-\theta_i)}} - \frac{1}{1 + e^{a_i \theta_i}},$$

and τ_i, k_i, r_i, c_i *are parameters.* $P(t)$ *accounts for external input to the excitatory subpopulation and* $Q(t)$ *external input to the inhibitory subpopulation of neurons. The equations are able to recreate periodic behavior observed in [27, 28]. We plot trajectories with different initial conditions in this state, see Figure 2.2. We also plot the solution corresponding to the red trajectory.*

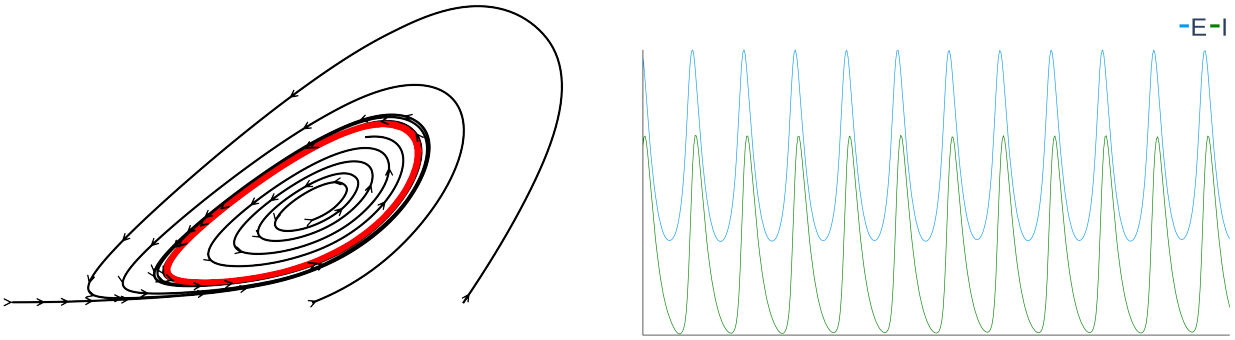

Figure 2.2 Dynamical system resulting from the Wilson-Cowan equations (Example 2.2.3). Left: The phase space M is illustrated in the IE-plane. We note how different trajectories tend to the red trajectory. Right: We plot the solution to the red trajectory. It clearly exhibits periodic behavior.

Representing a model in this way allows for a topological understanding of the system. This is done by looking at the trajectory in the phase space M. Although most systems can only be solved numerically, a general understanding of the shape formed in M provides qualitative information of the system [4]. In particular, knowing the topology of an attractor is of great significance. An attractor is a subset of M that pulls nearby trajectories into it.

Definition 2.2.4. *A set* $A \subset M$ *is called an attractor if*

1. *it is compact,*
2. *it is an invariant set, i.e. if* $a \in A$ *then* $\Phi(t, a) \in A$ *for all* $t \geq 0$,
3. *there is an invariant open neighborhood* U *of* A, *so that* $A = \bigcap_{t \geq 0} \{ \Phi(t, p) : p \in U \}$.

Example 2.2.5. *Consider the dynamical system given by the radial equation*

$$\dot{r} = r(1 - r^2), \qquad \dot{\theta} = 1$$

where $r \geq 0$. This system has a circle as an attractor in the xy-plane, shown in red in Figure 2.3.

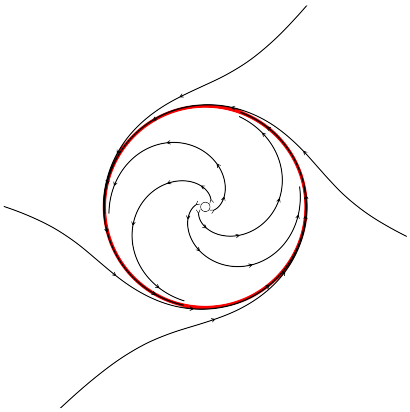

Figure 2.3 We depict trajectories of Example 2.2.5 in the xy-plane. The attractor of the system is shown in red.

Example 2.2.6. *Consider the van der Pol equation*

$$\ddot{x} + \mu(x^2 - 1)\dot{x} + x = 0$$

where $\mu \geq 0$ is a parameter. This system also has an attractor in the $x\dot{x}$-plane as shown in Figure 2.4. In this case, it is not a round unit circle, yet it is topologically equivalent to it.

An attractor that is homeomorphic to a circle correspond to a system exhibiting periodicity. In general, an attractor that is homeomporphic to an N-dimensional torus, a toroidal attractor, comes from a quasiperiodic system [5]. Quasiperiodicity has been widely documented in the scientific literature such as in fMRI of mice, electrocardiograms, crystal formation, and mammalian vocalization [10, 11, 8, 9]. Its presence is abundant in the real world. Moreover, it has also been shown to be a transition step between a chaos and stability [12, 13]. Mathematically:

Definition 2.2.7. *Let $\{\omega_i\}_{i=1}^N$ be positive incommensurate real numbers, i.e. $\omega_i \in \mathbb{R}_{>0}$ and they are linearly independent over $\mathbb{Q}$. We say that $f : \mathbb{R} \to \mathbb{C}$ is quasiperiodic with frequency vector*

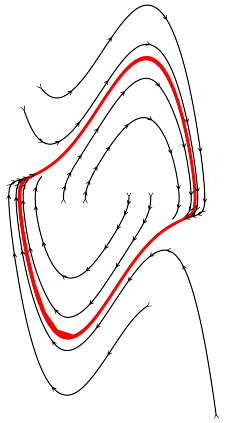

Figure 2.4 Trajectories of the van der Pol system in the $x\dot{x}$-plane. The attractor of the system is shown in red.

$\omega = (\omega_1, \ldots, \omega_N)$, *if*

$$f(t) = F(\omega_1 t, \ldots, \omega_N t),$$

where $F : \mathbb{T}^N \to \mathbb{C}$ *is a complex-valued continuous function on the* N*-torus* $\mathbb{T}^N = \mathbb{R}^N/\mathbb{Z}^N$*, called the parent function of* f.

In the case of a single frequency, f is just a periodic function. Thus, quasiperiodicity generalizes this notion. It is a recurrent behavior that can be detected in a time series, see Figure 2.5. In practice, one only has an observation of the dynamical system of interest in the form of a time series. The underlying equations governing the system are unknown i.e. we don't know M and in turn are unclear about Φ. Nevertheless, there is a way of reconstructing this unknown system while preserving qualitative information. Concretely, the remarkable 1981 result of Floris Takens assures us that a time series observation can be enough to reconstruct the topology of the original attractors [3].

Theorem 2.2.8 (**Taken's Embedding**). *Let* M *be a* m*-dimensional compact Riemannian manifold. For pairs* $(\phi, \bar{f})$*, where* $\phi \in C^2(M, M)$ *and* $\bar{f} \in C^2(M, \mathbb{R})$*, it is a generic property that the map* $\Phi_{\phi,\bar{f}} : M \to \mathbb{R}^{2M+1}$ *defined as*

$$\Phi_{\phi,\bar{f}}(p) = \left(\bar{f}(p), \bar{f}(\phi(p)), \bar{f}(\phi^2(p)), \ldots, \bar{f}(\phi^{2m}(p))\right)$$

is an embedding.

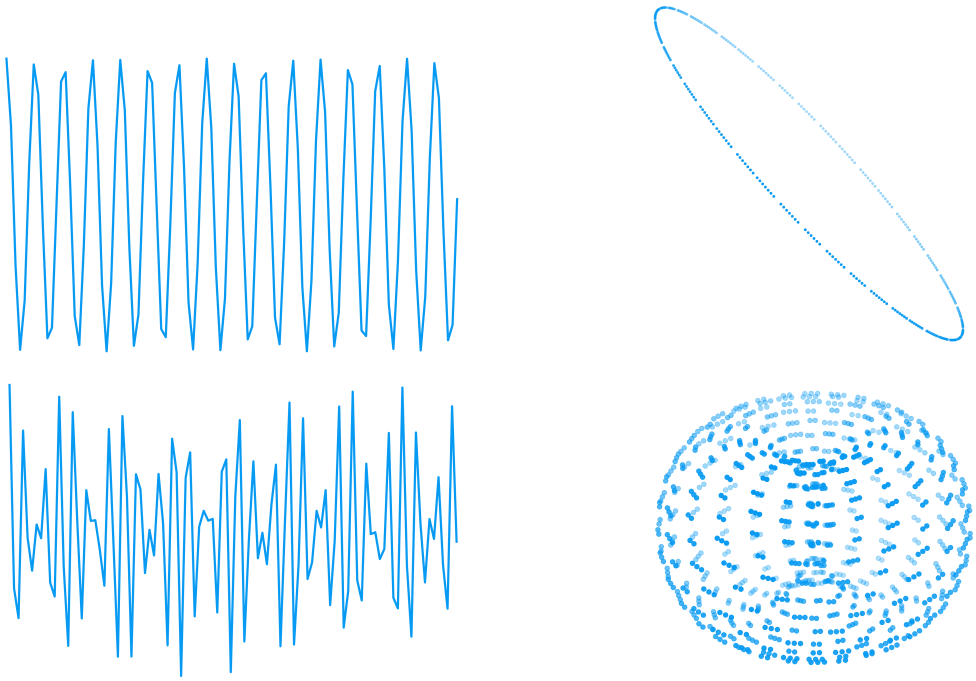

Figure 2.5 Top row: We illustrate a periodic signal on the left and show its sliding window embedding point cloud in three dimensions. Clearly, it lies on a circle. Bottom row: In this case we have a quasiperiodic signal generated with two incommensurate frequencies. This time, the embedding lies on a 2-dimensional torus.

Thus, our reconstruction may well look different than the original but we are assured it will be topologically equivalent. This is a powerful guarantee that validates the Sliding Window embedding technique (SW). This is a pipeline enabling the reconstruction of dynamical systems from a time series. In particular, it has been successfully used to detect quasiperiodicity [5, 6, 7].

Definition 2.2.9. *For a function $f : \mathbb{R} \to \mathbb{C}$, an integer $d > 0$ called the embedding dimension, and a real number $\tau > 0$ called the time delay, the sliding window embedding of f at t is given by:*

$$SW_{d,\tau} f(t) = \begin{bmatrix} f(t) \\ f(t+\tau) \\ \vdots \\ f(t+d\tau) \end{bmatrix} \in \mathbb{C}^{d+1}.$$

For $T \in \mathbb{N}$, we denote $\{SW_{d,\tau} f(t)\}_{t=0}^{T}$ as the sliding window point cloud. It follows by Takens' Theorem that for adequate choice of embedding dimension the sliding window point cloud will be

an embedding of M. Indeed, we interpret the time series f as the composition

$$f(t) = \bar{f}(\phi(0, p_t)),$$

where $\bar{f} : M \to \mathbb{C}$ is an observation function, $\phi : \mathbb{R} \times M \to M$ is the flow associated to Φ, and $p_t = \phi(t, p_0)$ for some $p_0 \in M$. Noting

$$f(t + i\tau) = \bar{f}(\phi(t, \phi(i\tau, p_0))) = \bar{f}(\phi(t, \phi^i(\tau, p_0))),$$

for $i \in \mathbb{N}$, justifies the claim.

Example 2.2.10. *Consider the Lorenz equations*

$$\dot{x} = \sigma(y - x)$$

$$\dot{y} = rx - y - xz$$

$$\dot{z} = xy - bz.$$

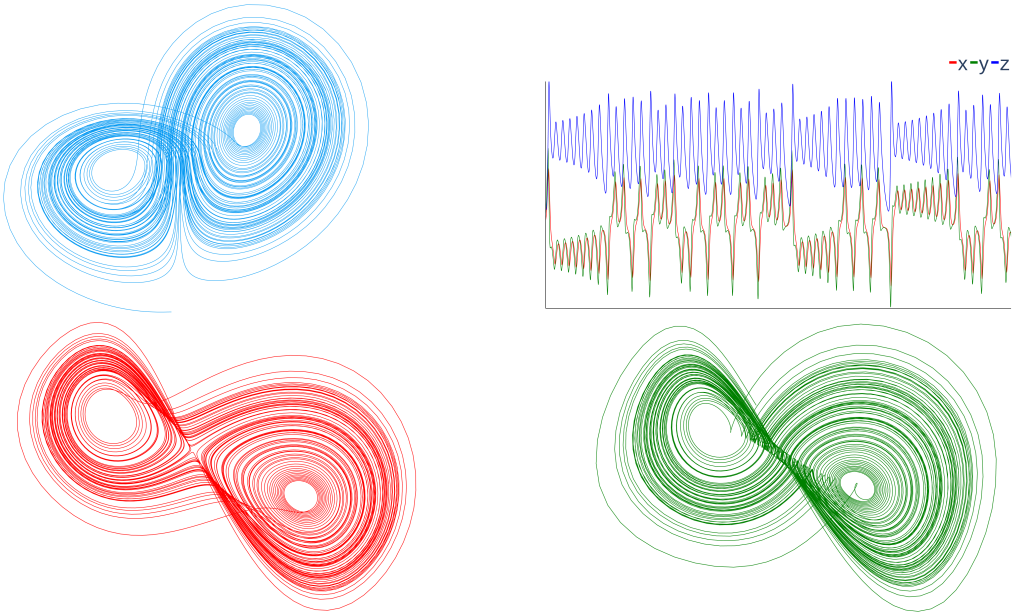

Figure 2.6 Top row: We depict the Lorenz system, Example 2.2.10, with parameter values $\sigma = 10, r = 28$, and $b = 8/3$. We note M is a bounded subset of $\mathbb{R}^3$. On the right we show the solution of the system for a particular initial condition. Bottom row: We use the solution of the system to reconstruct the phase space. Namely, on the left we have the result when using the embedding $SW_{d,\tau}x(t)$ and on the right when using $SW_{d,\tau}y(t)$.

This dynamical system exhibits fractal behavior in three dimensional space when $\sigma = 10, b = 8/3, r = 28$. *We reconstruct this behavior using the sliding window embedding map. We illustrate two different reconstructions by using* $x(t)$ *and* $y(t)$, *see Figure 2.6.*

For the reconstruction of quasiperiodic systems, an adequate choice of parameters d and τ is established in [5]. We are thus in the position of probing for recurrent behavior in a dynamical system by analyzing the sliding window point cloud of observed time series. The tool capable for the task is persistent homology as it provides a convenient geometrical representation at a multi-scale level. This leads to a robust approach capable of discerning noise and synthetic artifacts. In particular, for toroidal attractors, we are looking for homological features of an N-dimensional torus, as depicted in Figure 2.7. These steps constitute SW:

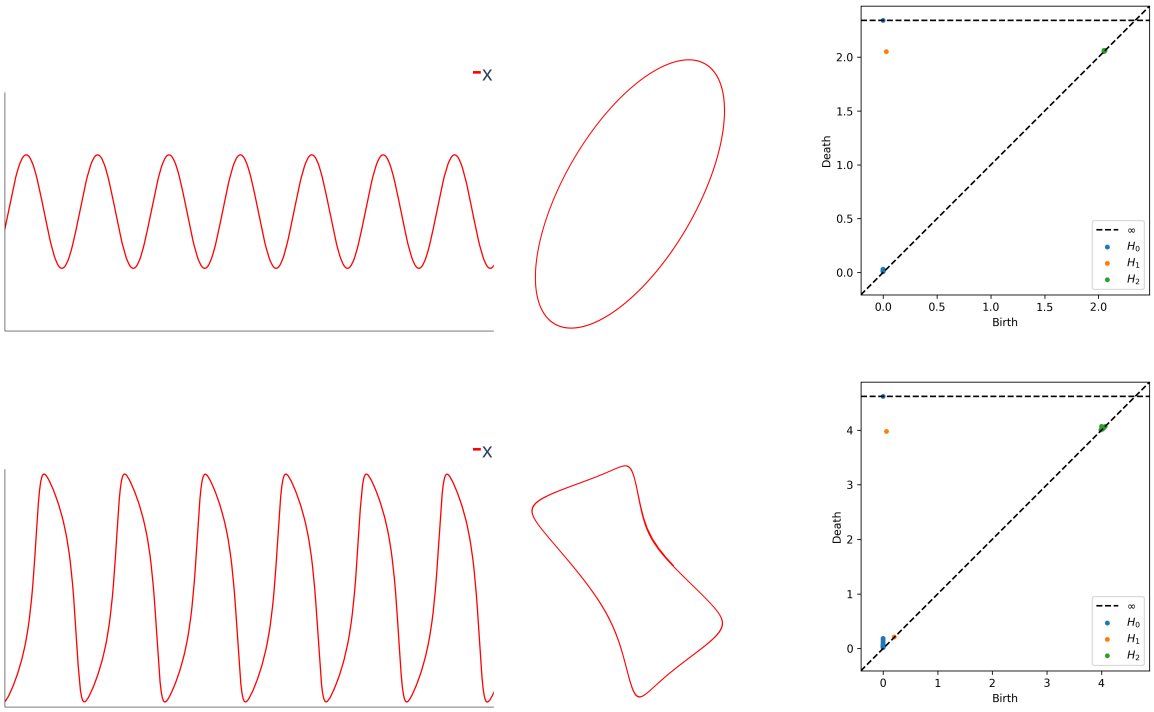

Figure 2.7 Top row: We perform SW to the radial system. The reconstruction is done using the $x(t)$ solution belonging to the attractor. Bottom row: SW to the van der Pol system. The reconstruction is also done using $x(t)$ of the trajectory corresponding to the attractor.

1. Start with a time series pertaining to a measurement of a system,
2. Construct the sliding window point cloud from it,

3. Compute their persistence diagrams to discern for the presence of an N-torus.

Example 2.2.11. *We illustrate SW by considering the radial equation and the van der Pol equation illustrated in Figure 2.3 and Figure 2.4, respectively. They both have an attractor that is topologically equivalent to the circle which translates to periodic behavior. Let us consider the solution of the attractor. Using $x(t)$ as input, we perform SW and reconstruct the attractor in three dimensions. As illustrated in Figure 2.7, both persistence diagrams show a persistent 1-dimensional feature and no significant 2-dimensional features. This is corresponds to the homology characterizing topologies equivalent to the circle.*

Although SW has been well established and found multiple applications [6, 7, 14], computing persistence diagrams is computationally taxing. This motivated our work of developing a faster alternative. We move on to cover the tools that helped us achieve this effort.

2.3 Fourier Series

For our purposes, we leverage the fast fourier transform (FFT) of time series data to infer the frequency vector. This is validated by theoretical results we present in this section. They can be found in [5].

Definition 2.3.1. *Let $\mathbb{T}$ be the quotient space $\mathbb{R}/(2\pi\mathbb{Z})$. For a single variable periodic function $g \in L^2(\mathbb{T})$ and $Z \in \mathbb{N}$, its Fourier series and its Z-truncated Fourier polynomial are written as*

$$g(t) = \sum_{k=-\infty}^{\infty} \hat{g}(k)e^{ikt} \quad \text{and} \quad S_Z g(t) = \sum_{k=-Z}^{Z} \hat{g}(k)e^{ikt}$$

where the Fourier coefficients of g are

$$\hat{g}(k) = \frac{1}{2\pi}\int_{-\pi}^{\pi} g(k)e^{-ikt}.$$

If g is continuously differentiable, one can show pointwise converge [29]. Let us now introduce the N-dimensional Fourier series.

Definition 2.3.2. *For $K \in \mathbb{N}$, let*

$$I_K^N = \{\mathbf{k} \in \mathbb{Z}^N \mid \|\mathbf{k}\|_\infty \leq K\},$$

where $\|\mathbf{k}\|_\infty = \max_i |k_i|$. *The K-truncated Fourier polynomial of* $F \in L^2(\mathbb{T}^N)$ *is the function*

$$S_K F(\mathbf{t}) = \sum_{\mathbf{k} \in I_K^N} \hat{F}(\mathbf{k}) e^{i\langle \mathbf{k}, \mathbf{t} \rangle}$$

where $\mathbf{t} \in \mathbb{R}^N$, $\langle \cdot, \cdot \rangle$ *is the standard inner product in* $\mathbb{R}^N$, *and*

$$\hat{F}(\mathbf{k}) = \frac{1}{(2\pi)^N} \int_0^{2\pi} \cdots \int_0^{2\pi} F(\mathbf{t}) e^{-i\langle \mathbf{k}, \mathbf{t} \rangle} dt_1 \cdots dt_N = \left\langle F, e^{i\langle \mathbf{k}, \cdot \rangle} \right\rangle_{L^2}$$

is the $\mathbf{k}$*-Fourier coefficient of F, for* $\mathbf{k} \in \mathbb{Z}^N$.

Analogously to the one dimensional case, the sequence $\{S_K F\}_{K \in \mathbb{N}}$ coverges to F in $L^2(\mathbb{T}^N)$ as $K \to \infty$. This analytical tool has been used to show the persistence diagrams obtained from a quasiperiodic function can be approximated in bottleneck distance with a truncated sum of exponentials. This result is paramount to the treatment of general quasiperiodic functions.

Theorem 2.3.3. *[5] Let* $f : \mathbb{R} \to \mathbb{C}$ *be a quasiperiodic function with frequency vector* ω *and parent function F. For* $\mathbf{k} \in \mathbb{Z}^N$ *and* $K \in \mathbb{N}$

$$\hat{F}(\mathbf{k}) = \lim_{\lambda \to \infty} \frac{1}{\lambda} \int_0^\lambda f(t) e^{-i\langle \mathbf{k}, t\omega \rangle} dt.$$

Furthermore, for $j \in \mathbb{N}$, $dgm_j^R(SW_{d,\tau} f)$ *can be approximated in bottleneck distance by*

$$dgm_j^R(SW_{d,\tau} S_K f) \qquad as \qquad K \to \infty,$$

where

$$S_K f(t) = \sum_{\|\mathbf{k}\|_\infty \leq K} \hat{F}(\mathbf{k}) e^{i\langle \mathbf{k}, t\omega \rangle}.$$

The approximation is of order $O\left(K^{\frac{N}{2} - r}\right)$ *when* $|\hat{F}(\mathbf{k})| = O(\|\mathbf{k}\|_2^{-r})$ *and* $r > N/2$.

This result allow us to focus on quasiperiodic functions that look like a sum of exponentials

$$f(t) = \sum_j c_j e^{i\omega_j t},$$

where $c_j \in \mathbb{C}$ and $\omega_j \in \mathbb{R}$. In this case the sliding window embedding can be expressed as $SW_{d,\tau} f(t) =$

$$\frac{1}{\sqrt{d+1}} \begin{pmatrix} 1 & \cdots & 1 \\ e^{i\omega_1 \tau} & \ddots & e^{i\omega_M \tau} \\ \vdots & \ddots & \vdots \\ e^{i\omega_1 d\tau} & \cdots & e^{i\omega_M d\tau} \end{pmatrix} \begin{pmatrix} \bar{c}_1 e^{i\omega_1 t} \\ \vdots \\ \bar{c}_M e^{i\omega_M t} \end{pmatrix} = A v_t,$$

where $\bar{c}_i = \sqrt{d+1}\, c_i$, $d \in \mathbb{N}$, and $\tau \in \mathbb{R}$. The vector v_t lies in a space homeomorphic to the N-torus, for some $N \leq M$; furthermore d and τ can be chosen for the same to hold for $SW_{d,\tau} f(t)$. Indeed, this was shown in [5] where it was concluded that N corresponds to the number of incommensurate frequencies.

The Cartesian product

$$G_T = \prod_j \{\bar{c}_j e^{i\omega_j t}\}_{t=0}^{T'}$$

offers a way of approximating $\{v_t\}_{t=0}^{T}$ in bottleneck distance via Theorem 2.1.14. This is useful since the persistence diagrams of G_T can be readily computed using the Persistent Künneth Formula. That this approach can also be used to approximate the sliding window embedding of f is presented in Theorem 4.3.1.

2.4 Continued Fraction Expansion

We now introduce a notion that is at the center of our method. It allow us to infer information from our frequency parameter and compute an approximation of the target persistence diagram. The idea is to express a number as a nested sequence of fractions. This can be achieved by a continued application of the division algorithm. For a rational number, this process will end after finitely many steps. We are primarily concerned with irrational numbers which have an infinite number of nested fractions. Definitions and results were retrieved from [18].

Definition 2.4.1. *Let ω be a positive irrational number. The continued fraction of ω is given by*

$$\omega = a_1 + \cfrac{1}{a_2 + \cfrac{1}{a_3 + \frac{1}{a_4 + \cdots}}} := [a_1, a_2, a_3, \cdots],$$

where $a_1 \in \mathbb{Z}$ and $a_i \in \mathbb{N}$, for $i > 1$.

As we alluded to, the expansion is infinite if and only if ω is irrational. Let us go over the iterative process to compute the expansion, namely to get the a_i's from ω. We denote by $\lfloor x \rfloor$ the floor function, i.e. the greatest integer less than x. We start by letting $a_1 = \lfloor \omega \rfloor$ and writing

$$\omega = a_1 + \frac{1}{x_2},$$

where x_2 is the irrational number given by

$$x_2 = \frac{1}{\omega - a_1}.$$

To calculate a_2 we note

$$\omega = a_1 + \frac{1}{\lfloor x_2 \rfloor + \frac{1}{x_3}},$$

where

$$x_3 = \frac{1}{x_2 - \lfloor x_2 \rfloor}.$$

Thus, $a_2 = \lfloor x_2 \rfloor$. Noticing the pattern, we can conclude that $a_i = \lfloor x_i \rfloor$ where

$$x_i = \frac{1}{x_{i-1} - \lfloor x_{i-1} \rfloor}$$

and $x_1 = \omega$.

Example 2.4.2. *Let us consider the case $\omega = \sqrt{2}$. Since*

$$x_2 = \frac{1}{\sqrt{2} - 1} = 2.41421\ldots,$$

$a_2 = \lfloor x_2 \rfloor = 2$. *Similarly, $a_3 = 2$ since*

$$x_3 = \frac{1}{2.41421\cdots - 2} = 2.41421\ldots.$$

In fact, this shows that for all i, $a_i = 2$, i.e.

$$\sqrt{2} = 1 + \frac{1}{2 + \frac{1}{2 + \frac{1}{2 + \cdots}}} = [1, 2, 2, \cdots].$$

Example 2.4.3. *The case $\omega = \sqrt{2}$ is an example of a quadratic irrational, namely a number of the form*

$$\frac{P \pm \sqrt{D}}{Q},$$

where P, Q, D are integers and D is positive and not a perfect square. Lagrange proved that these irrational numbers have periodic continued fractions, i.e. there exists a j_o such that $i > j_o$ implies

$$a_i = a_{i+r_o}$$

for some fixed $r_o \geq 1$. Indeed, as show for $\sqrt{2}$, this is true for $j_o = 1$ and $r_o = 1$. We denote periodic expansions with a bar above the repeating terms. With this notation, $\sqrt{2} = [1, \bar{2}]$. Similarly, one can readily show that

$$\frac{1 + \sqrt{10}}{3} = [\overline{1, 2, 1}],$$

in this case $j_o = 0$ and $r_o = 3$.

Example 2.4.4. *Gauss used a generalized notion of continued fractions to express the series [30]*

$$F(a, b, \gamma, x) = 1 + \sum_{i=0}^{\infty} \frac{\prod_{j=0}^{i}(a + j)(b + j)}{(i + 1)! \prod_{j=0}^{i}(\gamma + j)} x^{i+1}.$$

Using this result, one can readily obtain closed formulas for the continued fraction expansion of elementary functions. Indeed, one can show that for the positive integer n, the rational number $\frac{p}{q}$, where $gcd(p, q) = 1$, and $I_n(x)$ denoting the hyperbolic Bessel function of the first kind,

$$e^{1/n} = [1, n - 1, 1, 1, 3n - 1, 1, 1, 5n - 1, 1, 1, \dots],$$

$$\tanh(1/n) = [0, n, 3n, 5n, 7n, 9n, 11n, \dots],$$

and

$$\frac{I_{p/q}(2/q)}{I_{1+p/q}(2/q)} = [p + q, p + 2q, p + 3q, p + 4q, \dots].$$

From here onwards, we let ω denote a positive irrational number.

Definition 2.4.5. *Let $i \in \mathbb{N}$. The i-th convergent of ω is given by*

$$\frac{p_i}{q_i} = [a_1, a_2, \cdots, a_i].$$

The terms p_i and q_i play a special role in the theory. They can be obtained recursively thanks to the following result.

Proposition 2.4.6. *The numerators p_i and the denominators q_i of the i-th convergent of ω satisfy the equations*

$$p_i = a_i p_{i-1} + p_{i-2},$$

$$q_i = a_i q_{i-1} + q_{i-2}.$$

for $i \geq 1$, where

$$p_0 = 1, \qquad p_{-1} = 0,$$

$$q_0 = 0, \qquad q_{-1} = 1.$$

This provides a convenient computational avenue for obtaining the i-th convergent. It can also be used to show the following result.

Proposition 2.4.7. *p_i and q_i have no common divisor other than 1 or -1.*

We can also assert how good of an approximation they are to ω.

Proposition 2.4.8. *Let $i \geq 1$. Then*

$$\frac{1}{2q_i q_{i+1}} < \left|\omega - \frac{p_i}{q_i}\right| < \frac{1}{q_i q_{1+1}} < \frac{1}{q_i^2}.$$

Furthermore, this result allow us to establish the existence and uniqueness of infinite continued fraction expansions. Indeed, this follows by noting $q_i < q_{i+1}$ for all $i \geq 1$. This justifies the equality sign in the definition we presented. The next result illustrates more of the type of convergence. It characterizes subsequences converging from below and from above.

Proposition 2.4.9. *Let $i \geq 1$ be odd. Then*

$$\frac{p_i}{q_i} < \omega < \frac{p_{i+1}}{q_{i+1}}.$$

Example 2.4.10. *The results presented here can be used to argue the golden ration φ is the 'most' irrational number. Indeed, by noting*

$$\varphi = 1 + \frac{1}{1 + \frac{1}{1+\frac{1}{1+\cdots}}} = [1, 1, 1, \cdots],$$

one can show this expression corresponds to the slowest rate of convergence possible. Furthermore, the Klein diagram allow us to obtain a geometrical picture of the results presented, see Figure 2.8.

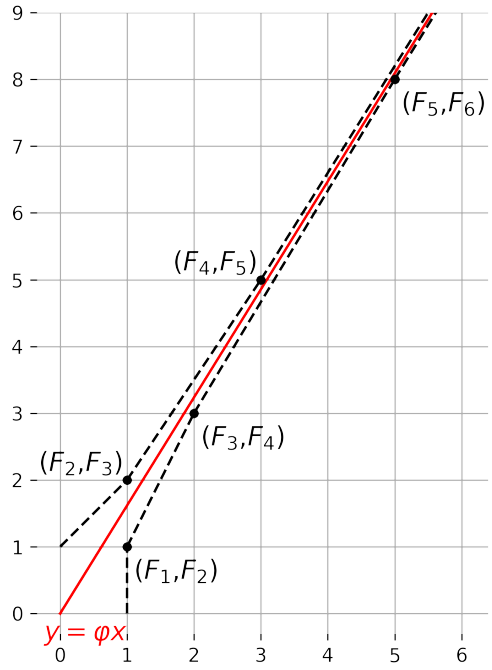

Figure 2.8 Klein diagram of the golden ratio.

We detailed how exponential functions play a critical role in the study of quasiperiodic functions. Let us consider a periodic function of the form

$$f(t) = e^{i\omega t}.$$

One can topologically describe $\{f(t)\}_{t=0}^{T}$ as a sampling of the circle. We can consider the analogues sampling using 'flat' coordinates.

Definition 2.4.11. *Let $N \in \mathbb{N}$ and $[x] = x \bmod 1$. We define the set*

$$S_{\omega,T} := \{[0], [\omega], \ldots, [T\omega]\}.$$

By identifying the endpoints of $[0, 1]$, this set can also be considered a sampling of the circle as shown in Figure 2.9. Furthermore, the function

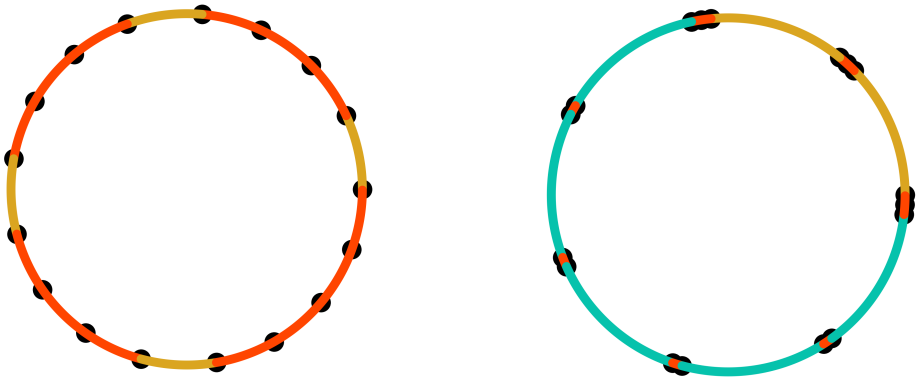

Figure 2.9 On the left we depict $S_{\pi-1,17}$. Each different gap size is shown in a different color. We note in this case there is only two gaps. On the right we show $S_{\sqrt{5},17}$. This case does have three different gaps.

$$\bar{d}(x, y) = \min\{|x - y|, |1 - y + x|, |1 - x + y|\}$$

defines a metric on this quotient space aligned with the notion of considering the space as a circle. It makes $(S_{\omega,T}, \bar{d})$ a metric space. As we will illustrate in this work, understanding $S_{\omega,T}$ is sufficient for the treatment of sampling of the form $\{f(t)\}_{t=0}^{T}$. The set $S_{\omega,T}$ is known in the literature as the Kronecker sequence. Its asymptotic behavior has been well documented [31]. Moreover, there is a remarkable result about this set: The Thee Gap Theorem, also known as the Steinhaus conjecture, it states [20]:

Theorem 2.4.12 (**Three Gap Theorem**). *Let $T \geq 1$. The points in $S_{\omega,T}$ partition $[0, 1]$ into $T + 1$ intervals, such that their lengths take at most 3 different values δ_A, δ_B and δ_C, with $\delta_C = \delta_A + \delta_B$.*

We note the result is independent of ω or T. Furthermore, the gaps from the theorem are closely related to the convergents of ω [32]. This forms the basis of our method, The Three Gap Theorem Method (3G), which consists in the application of the results of Theorem 4.2.1 and Theorem 4.3.2. We depict it schematically in Figure 2.10. It uses code, Algorithm 2.1, validated by The Three Gap Theorem to compute persistence diagrams that we then put back together using the Persistent

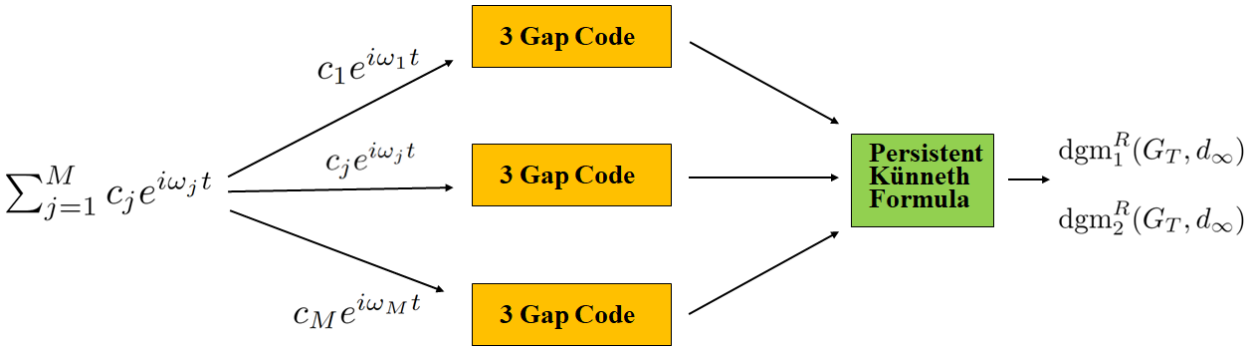

Figure 2.10 Schematic of our method 3G. We start with a sum of exponentials approximating a general quasiperiodic functions. The frequency parameters are retrieved using FFT. We apply our results to each frequency independently. We then put back the result using the Persistent Künneth formula in persistence homology. The result approximates a cross product space that is topologically similar to the sliding window point cloud of interest.

Algorithm 2.1 3 Gap Code

1: Input frequency ω_i
2: Scale frequency $\omega_i = \omega_i/(2\pi)$
3: Obtain continued fraction expansion, C.F.E., of ω_i
4: Use C.F.E. as shown in Theorem 4.2.1 to obtain gaps & their multiplicity
5: Scale gaps as detailed in Theorem 4.3.2 $[a, b) \to \bar{c}_i[\bar{a}, \bar{b})$
6: Output gaps

Künneth Formula. The resulting diagrams pertain to G_T which can approximate the sliding window point cloud of the quasiperiodic function of interest, see Theorem 4.3.1.

CHAPTER 3

STABILITY OF THE THREE GAP THEOREM IN PERSISTENCE DIAGRAMS

We begin by establishing the stability of The Three Gap Theorem in persistence diagrams. Our results validate the usage of the theorem in a computational setting. As a result we will establish the The Three Gap Theorem Method (3G) in the next chapter. Our stability results consist in looking at the number of matching continued fraction terms of two frequency values and the bottleneck distance of the corresponding sets. Furthermore, we present this stability in terms of the number of matching decimals of the two parameter values. Our results quantify the error one could expect when working with numerical approximations in this context.

3.1 Preliminaries

When a dynamical system transitions from a stable to a chaotic state, it undergoes an intermediary transition that exhibits repetitive like motions: quasiperiodicity [12]. The Sliding Window Embedding (SW) method has been successfully used for quasiperiodicity detection [5]. It consists in reconstructing a time series using the sliding window map and then computing the persistence homology of the reconstruction. Since the reconstruction of a quasiperiodic signal with N incommensurable frequencies will span a N dimensional torus, the geometric characterisation provided by looking at the persistence diagram is of most value. However, obtaining this information is computationally taxing and is thus limited to small sample sizes. This was the motivation for an approximation alternative: The Three Gap Theorem Method (3G). This avenue provides a much quicker and computationally feasible approach allowing for scaling of the sample size [33]. To achieve this, we leverage the continued fraction expansion of the frequency parameters. This is possible due to the Three Gap Theorem [20]. The theorem is depicted in Figure 3.1. Being the basis of our approximation method, we begin by validating its stability. As shown in Figure 3.1, two different sampling parameters close in norm can have very different outcomes. Our work addresses this issue by providing a better stability condition, namely decimal precision. Indeed, denoting $x_j = \frac{\lfloor 10^j \omega \rfloor}{10^j}$, the first j decimal terms of ω, we prove

Theorem 3.2.9 *Suppose*

$$x_j = \bar{x}_j$$

for some $j \in \mathbb{N}$. *If* $0 < T < q_{k_j(\omega)-1}$, *then for* $i \geq 0$

$$d_B(dgm_i^R(S_{\omega,T}), dgm_i^R(S_{\bar{\omega},T})) = O(k_j(\omega)^{-1}) \quad as\ j \to \infty.$$

The function $k_j(\omega)$ is a non-decreasing function that allow us to connect continued fraction expansion precision with decimal precision. Furthermore, we can also state the rate of decay of the bottleneck distance of two persistence diagrams as we increase decimal precision

Theorem 3.2.10 *For* $0 < \epsilon < z_0$ *there exists positive constants* C, λ *(depending on* ϵ*) with* $0 < \lambda < 1$ *such that for all integers* $j \geq 1$ *for which*

$$x_j = \bar{x}_j,$$

and $T < q_{k_j(\omega)-1}$, *if* $k_j(\omega) \geq jz_0$, *then for* $i \geq 0$

$$P\left(d_B(dgm_i^R(S_{\omega,T}), dgm_i^R(S_{\bar{\omega},T})) \leq \frac{1}{j(\epsilon + z_0)}\right) \leq C\lambda^j,$$

otherwise

$$P\left(d_B(dgm_i^R(S_{\omega,T}), dgm_i^R(S_{\bar{\omega},T})) \leq \frac{1}{j(z_0 - \epsilon)}\right) \geq 1 - C\lambda^j.$$

This exponential decay is exhibited in Figure 3.3 and Figure 3.4. It is a valuable guaranteed since 3G entails using the fast Fourier transform to retrieve frequencies. We can now proceed knowing the error we could expect given a sample size.

3.2 Stability Results

3.2.1 Stability with respect to C.F.E.

We begin by working with the continued fraction expansion of two parameter values. For what follows, we let ω and $\bar{\omega}$ denote two positive irrational numbers. We denote their i-th continued fraction terms and j-th convergents by $a_i, \bar{a}_i$ and $p_j/q_j, \bar{p}_j/\bar{q}_j$, respectively.

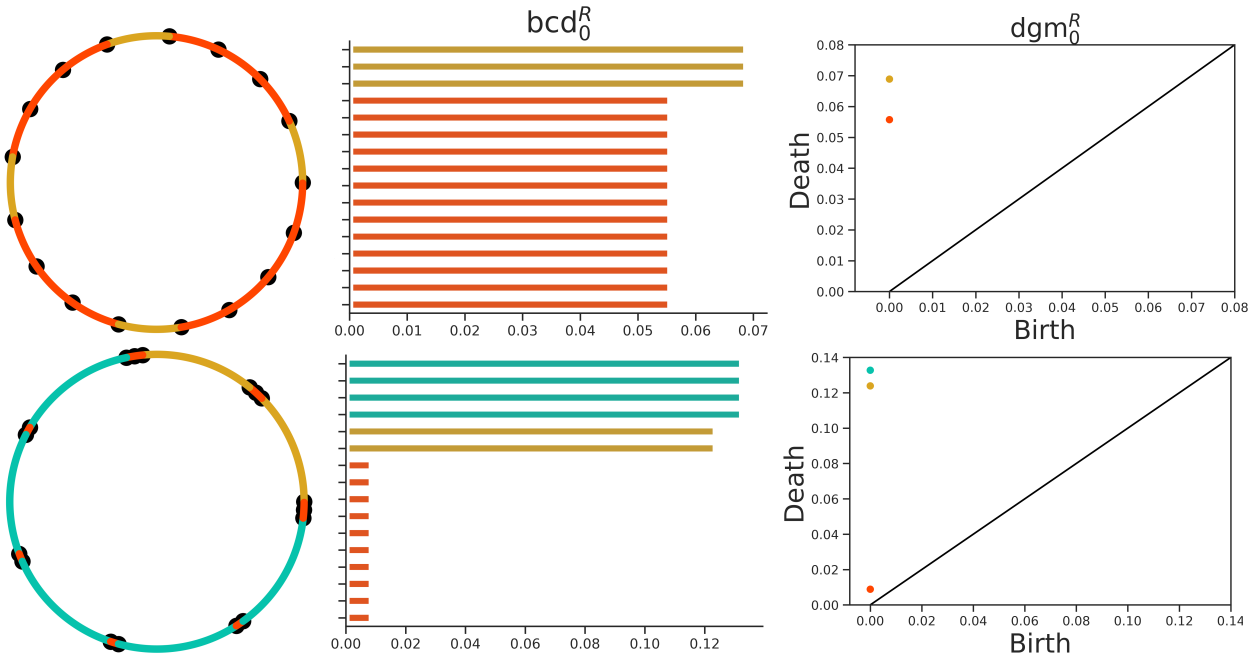

Figure 3.1 We illustrate the result of the three gap theorem and how they translates directly to results in persistence homology. Top row: The set $S_{\pi-1,17}$ is illustrated with the two gaps it creates. Bottow row: The set $S_{\sqrt{5},17}$ creates three gaps. Due to clustering, it is a poor covering of the circle. We note $d_2(\pi - 1, \sqrt{5}) = 0.094$.

Proposition 3.2.1. *Suppose there exists a $j \in \mathbb{N}$ such that $a_i = \bar{a}_i$ for all $i \leq j$. If $0 < T < q_{j-1}$,*

$$T|\omega - \bar{\omega}| < \frac{1}{q_j}.$$

Proof. W.L.O.G we assume $\omega < \bar{\omega}$. If $j-1$ is even, $\frac{p_{j-1}}{q_{j-1}} \leq \omega < \bar{\omega}$. Since $|\bar{\omega} - \frac{\bar{p}_{j-1}}{\bar{q}_{j-1}}| < \frac{1}{\bar{q}_{j-1}\bar{q}_j}$ and noting $q_i = \bar{q}_i$, $p_i = \bar{p}_i$ for all $i \leq j$, we conclude

$$|\omega - \bar{\omega}| = \bar{\omega} - \omega < \bar{\omega} - \frac{\bar{p}_{j-1}}{\bar{q}_{j-1}} < \frac{1}{q_{j-1}q_j}.$$

Similarly, if $j-1$ is odd we note $\omega < \bar{\omega} \leq \frac{\bar{p}_{j-1}}{\bar{q}_{j-1}} = \frac{p_{j-1}}{q_{j-1}}$. Using $|\omega - \frac{p_{j-1}}{q_{j-1}}| < \frac{1}{q_{j-1}q_j}$, we conclude

$$|\omega - \bar{\omega}| < \frac{p_{j-1}}{q_{j-1}} - \omega < \frac{1}{q_{j-1}q_j}.$$

Thus,

$$T|\omega - \bar{\omega}| < \frac{q_{j-1}}{q_j q_{j-1}} = \frac{1}{q_j}.$$

□

Corollary 3.2.2. *Suppose there exists a $j \in \mathbb{N}$ such that $a_i = \bar{a}_i$ for all $i \leq j$. If $0 < T < q_{j-1}$,*

$$\bar{d}([r\omega], [r\bar{\omega}]) < \frac{1}{q_j}$$

where $r \in \mathbb{N}$ and $r \leq T$.

Proof. By the previous lemma, we note

$$T|\omega - \bar{\omega}| < \frac{1}{q_j} \ \leq \ \frac{1}{2}.$$

This implies that for $r \in \mathbb{N}$ and $r \leq T$

$$\bar{d}([r\omega], [r\bar{\omega}]) = r|\omega - \bar{\omega}|.$$

The result follows. □

Corollary 3.2.2 provides us with a matching of $S_{\omega,T}$ and $S_{\bar{\omega},T}$ such that pairs have a distance less than $1/q_j$. This translates to an upper bound of $d_H(S_{\omega,T}, S_{\bar{\omega},T})$. Moreover, by translating one of the sets by a factor of $T|\omega - \bar{\omega}|/2$ we obtain an analogues bound for $d_{GH}(S_{\omega,T}, S_{\bar{\omega},T})$:

Proposition 3.2.3. *Suppose there exists a $j \in \mathbb{N}$ such that $\omega_i = \bar{\omega}_i$ for all $i \leq j$. If $0 < T < q_{k-1}$, then*

$$d_{GH}(S_{\omega,T}, S_{\bar{\omega},T}) \leq \frac{1}{2q_j}.$$

Proof. W.L.O.G. we assume $\omega < \bar{\omega}$. Consider the function $f : [0, 1) \to [0, 1)$ given by

$$f(x) = \left[x - \frac{T|\omega - \bar{\omega}|}{2}\right].$$

Clearly, f is an isometry. Furthermore, since $\frac{T|\omega-\bar{\omega}|}{2} < \frac{1}{2}$, we note that for $r \in \mathbb{N}$ and $r \leq T$

$$\bar{d}(f([r\bar{\omega}]), [r\omega]) = \left|\bar{d}([r\bar{\omega}], [r\omega]) - \frac{T|\omega - \bar{\omega}|}{2}\right| \leq \frac{T|\omega - \bar{\omega}|}{2}.$$

Thus,

$$d_H(f(S_{\bar{\omega},T}), S_{\omega,T}) \leq \frac{T|\omega - \bar{\omega}|}{2} < \frac{1}{2q_j}.$$

This shows the result. □

We can then apply Theorem 2.1.14 to conclude the next result.

Corollary 3.2.4. *Suppose there exists a $j \in \mathbb{N}$ such that $\omega_r = \bar{\omega}_r$ for all $r \leq j$. If $0 < T < q_{k-1}$, then for $i \geq 0$*

$$d_B(dgm_i^R(S_{\omega,T}), dgm_i^R(S_{\bar{\omega},T})) \leq \frac{1}{q_k}.$$

Our results up to now have been with respect to continued fraction expansions. We are able able to relate them to decimal precision using the function $k_i(\omega)$ which takes the first i-th terms in the decimal expansion of ω and returns the number of matching partial quotients of the continued fraction expansion of ω.

3.2.2 Stability with respect to Decimal Precision

We introduce the function $k_i(\omega)$ by presenting examples on how to compute it. To do so, we need two decimals

$$x_i = \frac{\lfloor 10^i \omega \rfloor}{10^i} \quad \text{and} \quad y_i = x_i + \frac{1}{10^i},$$

where $\lfloor \omega \rfloor$ denotes the floor of ω. We obtain $k_i(\omega)$ by tracking the number of the first matching quotients in the continued fraction expansions of x_i and y_i.

For example, consider $\omega = \sqrt[3]{7} = 1.91293118....$ To compute $k_3(\omega)$ we note

$$x_3 = 1.912 \quad \text{and} \quad y_3 = 1.913,$$

Their continued fraction expansions are $[1, 1, 10, 2, 1, 3]$ and $[1, 1, 10, 2, 43]$, respectively. Thus, $k_3(\sqrt[3]{7}) = 3$. Similarly, for $k_6(\omega)$ we note

$$x_6 = 1.912931 \quad \text{and} \quad y_6 = 1.912932,$$

Their respective continued fraction expansions are $[1, 1, 10, 2, 16, 3, 21, 4, 2]$ and $[1, 1, 10, 2, 16, 2, 11, 2, 1, 2, 3]$. Thus, $k_6(\sqrt[3]{7}) = 4$.

For a fixed ω, the function $k_i(\omega)$ can always be computed using these steps. Furthermore, this function has been well studied in the past [34]:

Theorem 3.2.5. *For almost all irrationals ω, with respect to Lebesgue measure, we have*

$$\lim_{i \to \infty} \frac{k_i(\omega)}{i} = \frac{6\, log(10)\, log(2)}{\pi^2}.$$

We denote the limit above by z_0 and apply a more recent result to our work [35]:

Theorem 3.2.6. *For all $\epsilon > 0$, there exists positive constants C, λ (depending on ϵ) with $0 < \lambda < 1$ such that*

$$P\left(\left|\frac{k_i(\omega)}{i} - z_0\right| \geq \epsilon\right) \leq C\lambda^i$$

for all integers $i \geq 1$.

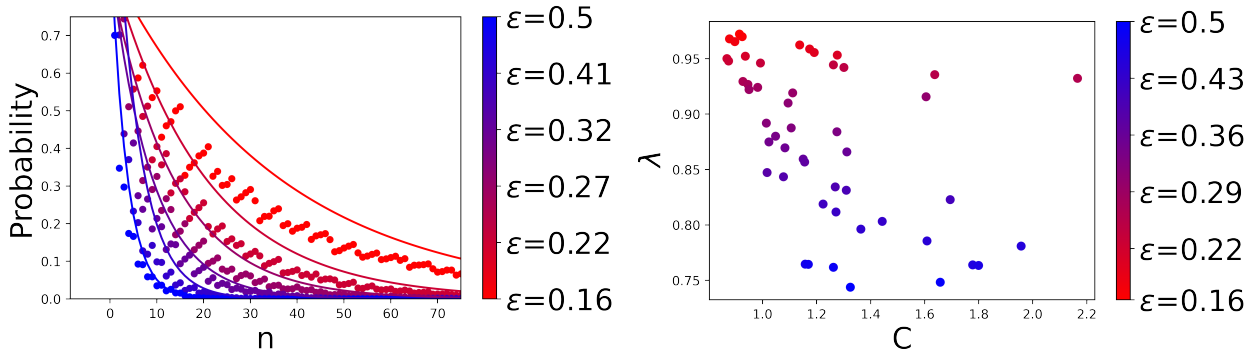

Figure 3.2 We illustrate the result of Theorem 3.2.6. We compute the k_i function for 5,000 values of ω. These are obtained from sampling the interval (0,1) uniformly.

We now relate the k function to our work. The following lemma is obtained by construction. Let us denote by $\bar{x}_j$ the decimal obtained from $\bar{\omega}$.

Lemma 3.2.7. *Suppose*

$$x_j = \bar{x}_j$$

for some $j \in \mathbb{N}$. Then $a_r = \bar{a}_r$ for all $r \leq k_j(\omega)$.

We can now combined our previous results to obtain a relation in terms of decimal precision:

Proposition 3.2.8. *Suppose*

$$x_j = \bar{x}_j$$

for some $j \in \mathbb{N}$. If $0 < T < q_{k_j(\omega)-1}$, then for $i \geq 0$

$$d_B(dgm_i^R(S_{\omega,T}), dgm_i^R(S_{\bar{\omega},T})) \leq \frac{1}{q_{k_j(\omega)}}.$$

This provides us with a rate of decay for the bottleneck distance. We further simplify this observation by noting that $q_{k_j(\omega)} \geq k_j(\omega)$.

Theorem 3.2.9. *Suppose*

$$x_j = \bar{x}_j$$

for some $j \in \mathbb{N}$. *If* $0 < T < q_{k_j(\omega)-1}$, *then for* $i \geq 0$

$$d_B(dgm_i^R(S_{\omega,T}), dgm_i^R(S_{\bar{\omega},T})) = O(k_j(\omega)^{-1}) \qquad as\ j \to \infty.$$

We can further obtain a relation illustrating the rate at which the bottleneck distance decays.

Theorem 3.2.10. *For* $0 < \epsilon < z_0$ *there exists positive constants* C, λ *(depending on* ϵ*) with* $0 < \lambda < 1$ *such that for all integers* $j \geq 1$ *for which*

$$x_j = \bar{x}_j$$

and $T < q_{k_j(\omega)-1}$, *if* $k_j(\omega) \geq jz_0$, *then for* $i \geq 0$

$$P\Big(d_B(dgm_i^R(S_{\omega,T}), dgm_i^R(S_{\bar{\omega},T})) \ \leq \frac{1}{j(\epsilon + z_0)}\Big) \leq \ C\lambda^j,$$

otherwise

$$P\Big(d_B(dgm_i^R(S_{\omega,T}), dgm_i^R(S_{\bar{\omega},T})) \ \leq \frac{1}{j(z_0 - \epsilon)}\Big) \geq \ 1 - C\lambda^j.$$

Proof. Let $\epsilon > 0$. By Theorem 3.2.6 there exists positive constants C, λ (depending on ϵ) with $0 < \lambda < 1$ such that

$$P\Big(\Big|k_j(\omega) - jz_0\Big| \geq j\epsilon\Big) \leq \ C\lambda^j.$$

If $k_j(\omega) \geq jz_0$ this implies

$$P\Big(\frac{1}{k_j(\omega)} \leq \frac{1}{j\epsilon + jz_0}\Big) \leq \ C\lambda^j,$$

combined with Theorem 3.2.8 give the first half of the result. If $k_j(\omega) < jz_0$ we can use the inequality, following from Theorem 3.2.6 as well,

$$P\Big(\Big|k_j(\omega) - jz_0\Big| < j\epsilon\Big) \geq \ 1 - C\lambda^j,$$

to conclude

$$P\Big(\frac{1}{k_j(\omega)} \leq \frac{1}{jz_0 - j\epsilon}\Big) \geq 1 - C\lambda^j$$

since $jz_0 - j\epsilon > 0$. Similarly, applying Theorem 3.2.8 shows the second part of the result and completes the proof. □

3.3 Applications

We now analyze the error in computations using our main results. We detail their application when retrieving frequencies using the Fast Fourier Transform (FFT) and when dealing with quasiperiodic signals.

3.3.1 Fast Fourier Transform

We illustrate the approach by considering a signal of the form

$$f_\omega(t) = e^{it\omega}.$$

As shown in [5], this type of signal is related to a periodic dynamical system. In practice, the frequency ω is approximated using FFT, say $\bar{\omega}$, and thus it is subject to error. Since 3G relies on this information to approximate the SW obtained from the original signal, we can apply our work to keep track of the stability of the method.

Let's consider the case

$$\omega_1 = \sqrt{3} = 1.7320508075688772...$$

and that we are able to recover four decimals of precision, say

$$\omega_2 = 1.7320641266595873... .$$

The Three Gap Theorem method will use the frequencies, as shown in 4.3.2,

$$\omega = \frac{\omega_1}{2\pi} = 0.27566444771089604...$$

and

$$\bar{\omega} = \frac{\omega_2}{2\pi} = 0.27566656751002... .$$

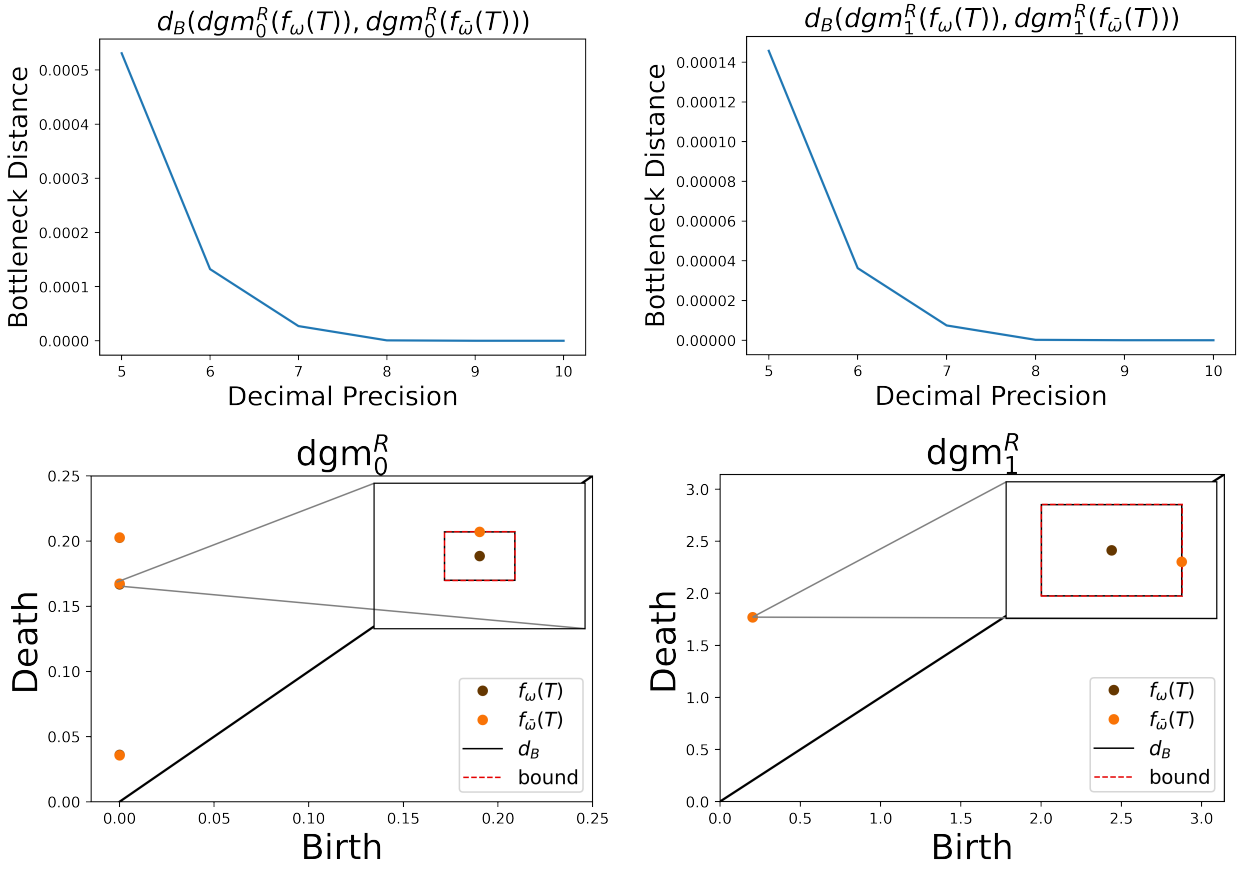

Figure 3.3 We depict the results from 3.3.1 where $T = \{0, 1, ..., 43\}$. **Top Row:** We plot the change of the bottleneck distance as we add more decimals of precision to $\bar{\omega}$. **Bottom Row:** Depicted are the pairs achieving the bottleneck distance. We note our bound is almost identical to the bottleneck distance.

In this case, $x_5 = \bar{x}_5$, $k_5(a) = 7$, $q_6 = 43$, and $q_7 = 51$. Thus, by Theorem 3.2.8, for $i \geq 0$

$$d_B(dgm_i^R(S_{\omega,43}), dgm_i^R(S_{\bar{\omega},43})) \leq \frac{1}{51} = 0.01960....$$

Furthermore, we can compute the exact distance in dimension 0 and 1, say ϵ_0, ϵ_1, respectively, using the results from 4.2.2. We can then obtain the bound

$$d_B(dgm_0^R(f_\omega(T)), dgm_0^R(f_{\bar{\omega}}(T)) = 5.3089 \times 10^{-4} \leq 2\pi\epsilon_0 = 5.3277 \times 10^{-4}$$

and

$$d_B(dgm_1^R(f_\omega(T)), dgm_1^R(f_{\bar{\omega}}(T)) = 1.4574 \times 10^{-4} \leq 2\pi\epsilon_1 = 1.4651 \times 10^{-4},$$

where $T = \{0, 1, ..., 43\}$. This follows by noting that to recover distances in the complex plane we can use the map $x \longrightarrow 2\sin(\pi x)$ as illustrated in 4.3. Furthermore, since

$$2\sin(\pi x) - 2\sin(\pi y) \leq 4\sin(\frac{\pi(x-y)}{2}) \leq 2\pi(x-y),$$

using $(x - y) << 1$, the upper bounds follow. Moreover, by combining these observations with Theorem 3.2.8, we note

$$d_B(dgm_i^R(f_\omega(T)), dgm_i^R(f_{\bar{\omega}}(T))) \leq \frac{2\pi}{q_7}.$$

3.3.2 Quasiperiodic Functions

We now apply a similar analysis to the more complicated quasiperiodic signal

$$f_\omega(t) = e^{it} + e^{it\omega}.$$

In this case, 3G consists in constructing a Cartesian product space to approximate $\left\{SW_{d,\tau}(f_\omega(t))\right\}_{t=0}^{T}$, see 4.3. For this example, we denote the Cartesian product space as

$$G_{\omega,T} = \{e^{it}\}_{t=0}^{T} \times \{e^{it\omega}\}_{t=0}^{T}$$

The persistence of this Cartesian product space can be computed using the persistence Künneth formula [14] and the results in 4.3. We highlight that doing so does not require Ripser at any point. Our error analysis consists in varying the decimal precision of ω to obtain a $\bar{\omega}$. We then compare the bottleneck distance as before but now of the sets $G_{\omega,T}$ and $G_{\bar{\omega},T}$. Furthermore, as a direct consequence of the Künneth formula, we can obtain analogue bounds to the ones in Section 3.3.1:

$$d_B(dgm_1^R(G_{\omega,T}), dgm_1^R(G_{\bar{\omega},T})) \leq 2\pi\lambda_1$$

and

$$d_B(dgm_2^R(G_{\omega,T}), dgm_2^R(G_{\bar{\omega},T})) \leq 2\pi\lambda_2,$$

where $\lambda_j = d_B(dgm_j^R(S_{\frac{1}{2\pi},T} \times S_{\omega,T}), dgm_j^R(S_{\frac{1}{2\pi},T} \times S_{\bar{\omega},T}))$, which can be computed directly using 3G.

Let us consider the case $\omega = \sqrt{5}$ and say we approximate with precision of five decimals $\bar{\omega} = 2.23606$. Computing ω and $\bar{\omega}$ as before, we obtain $x_5 = \bar{x}_5$, $k_5(\omega) = 7$, $q_6 = 100$, and $q_7 = 121$. To apply our results from Theorem 3.2.8 to the bound above, we let $T = 100$. Noting the bound, for $j = 1, 2$,

$$\lambda_j \leq \max\{\epsilon_0, \epsilon_1\},$$

where ϵ_i is as defined in Section 3.3.1, we conclude that

$$d_B(dgm_j^R(G_{\omega,T}), dgm_j^R(G_{\bar{\omega},T})) \leq \frac{2\pi}{q_7}.$$

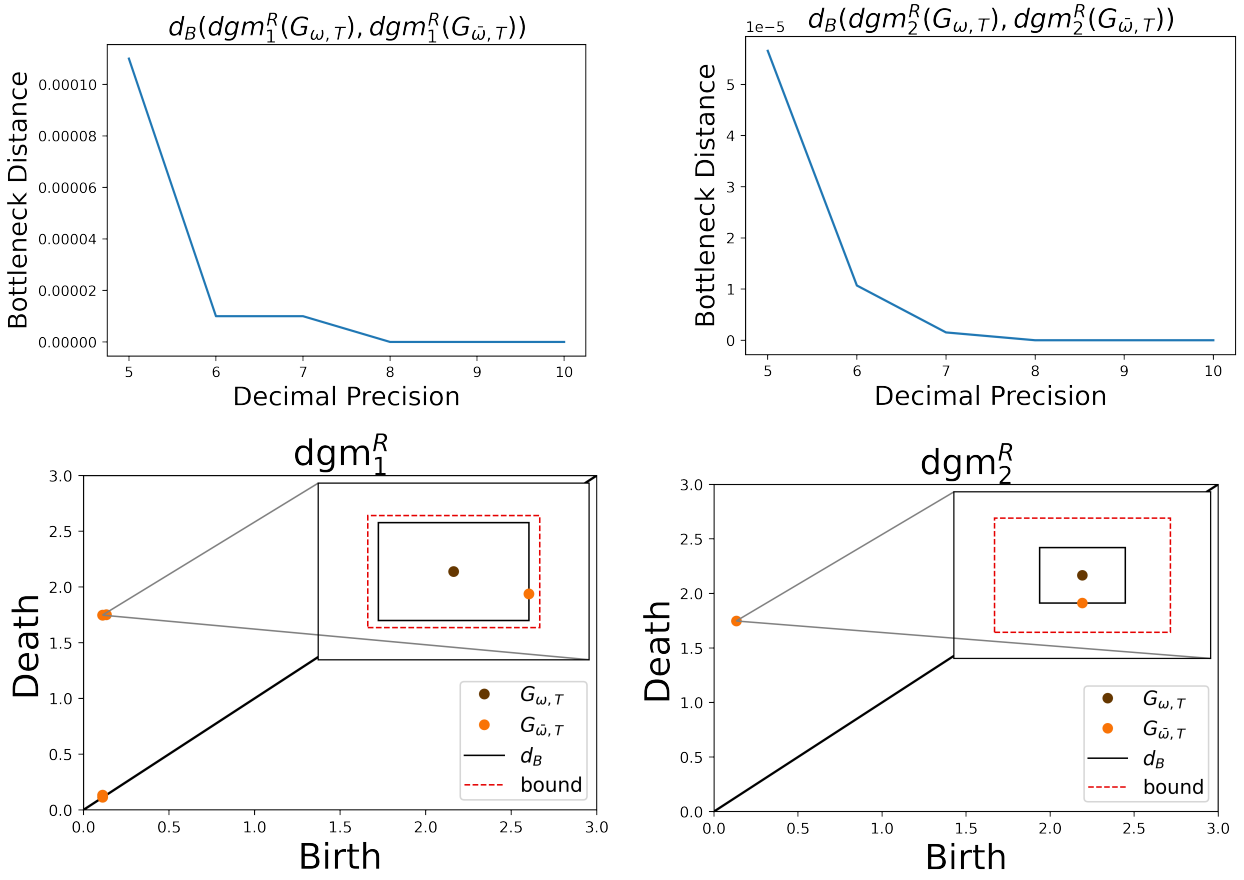

Figure 3.4 We depict the results from 3.3.2. **Top Row:** We plot the change of the bottleneck distance as we add more decimals of precision to $\bar{\omega}$. **Bottom Row:** Depicted are the pairs achieving the bottleneck distance. We note our bound is still close to the bottleneck distance.

3.4 Concluding Remarks

We have successfully presented stability results that validate the use of The Three Gap Theorem method under an adequate sample size. Furthermore, we are able to quantify the divergence in the outcome of the approximation. This is relative to the number of matching continued fraction exponents. It can also be related to decimal precision thanks to the introduction of the k_j function. Overall, we hope this work helps in the further implementation of 3G and on its role of better understanding and detecting quasiperiodic signals.

CHAPTER 4

ESTIMATION OF PERSISTENCE DIAGRAMS VIA THE THREE GAP THEOREM

We present theoretical and computational schemes to approximate the persistence diagrams of sliding window embeddings from quasiperiodic functions. We do so by combining the Three Gap Theorem from number theory, the Persistent Künneth formula from TDA, and our stability results to and derive fast and provably correct persistent homology approximations. The input to our procedure is the spectrum of the signal, and we provide numerical evidence of its utility to capture the shape of toroidal attractors.

4.1 Preliminaries

Figure 4.1 depicts a system with a behavior more complex than periodicity. By using any

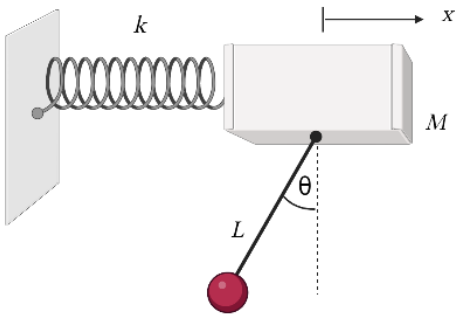

Figure 4.1 Pendulum attached to a sliding block.

measurement of the system, say the horizontal position $x(t)$ or the angular position $\theta(t)$, we can determine the qualitative aspects of the system and conclude it exhibits an oscillatory pattern. Currently, a significant limitation is the computational time it takes to analyze the reconstructed signal. Our work addresses this issue by detailing an estimation method of the standard approach capable of proving results orders of magnitude faster. Explicitly, we provide an alternative to step 3 below, depicted in Figure 4.2:

1. Start with an observation signal f.

2. Reconstruct the phase space by computing $\{SW_{d,\tau}f(t)\}_{t=0}^{T}$.

~~3.~~ Compute $\mathrm{dgm}_j^R(\{SW_{d,\tau}f(t)\}_{t=0}^{T}, d_2)$ using **Ripser**.

3. (a) Use the FFT to retrieve the frequencies of f and then use them to compute continued fraction expansions.

(b) Use them as shown in Section 4.2 and then apply the results from Section 4.3 to approximate $\mathrm{dgm}_j^R(\{SW_{d,\tau}f(t)\}_{t=0}^{T}, d_2)$.

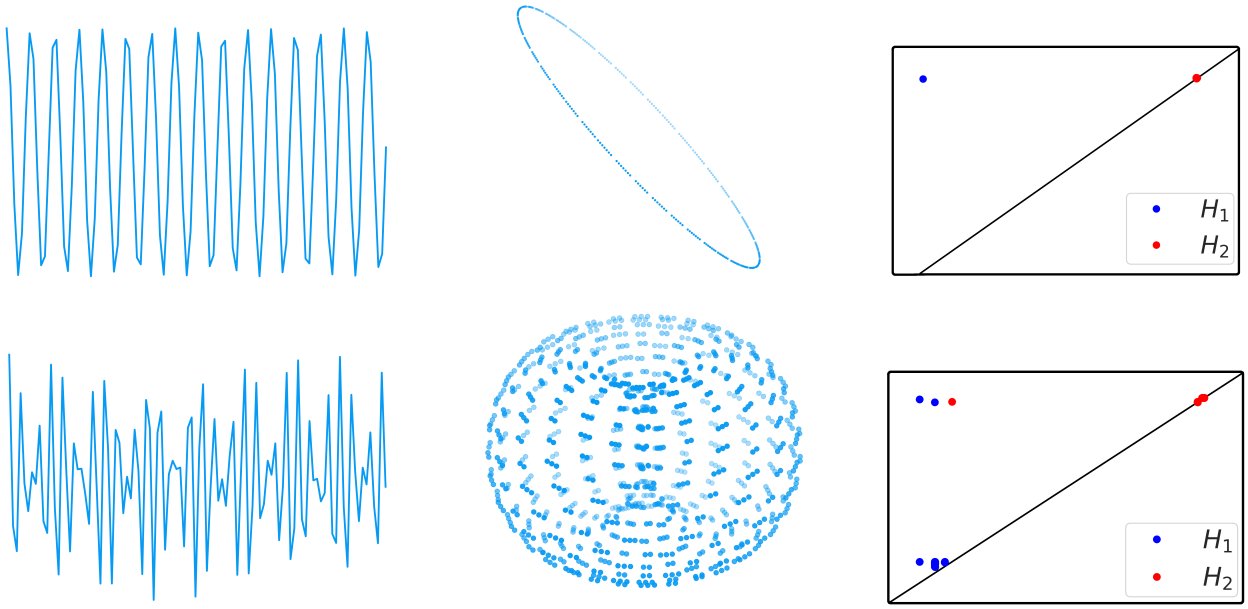

Figure 4.2 The SW starts with a signal, followed by a reconstruction of the phase space, and concludes with the computation of persistent homology. Top row: Signal obtained from the periodic motion of an ideal pendulum. The sliding window point cloud recovers a circle, hence its persistence diagram only has one hole in dimension 1. Bottom row: A quasiperiodic function with two incommensurate frequencies (left), a PCA projection of its sliding window embedding (center) recovers a 2-torus. The persistence diagrams verify this topology: two 1-dim holes, and one 2-dim hole.

4.2 Main Results

Let us consider the Kronecker Sequence with one parameter $S_{\omega,N}$. We note $(S_{\omega,T}, \bar{d})$ is a metric space and that the distribution of points in $S_{\omega,T}$ can behave drastically different for parameters close in d_2.

4.2.1 Persistence Diagrams

We are able to compute $\mathrm{dgm}_0^R(S_{\omega,T}, \bar{d})$ applying the information from The Three Gap Theorem which involves the i-th convergents.

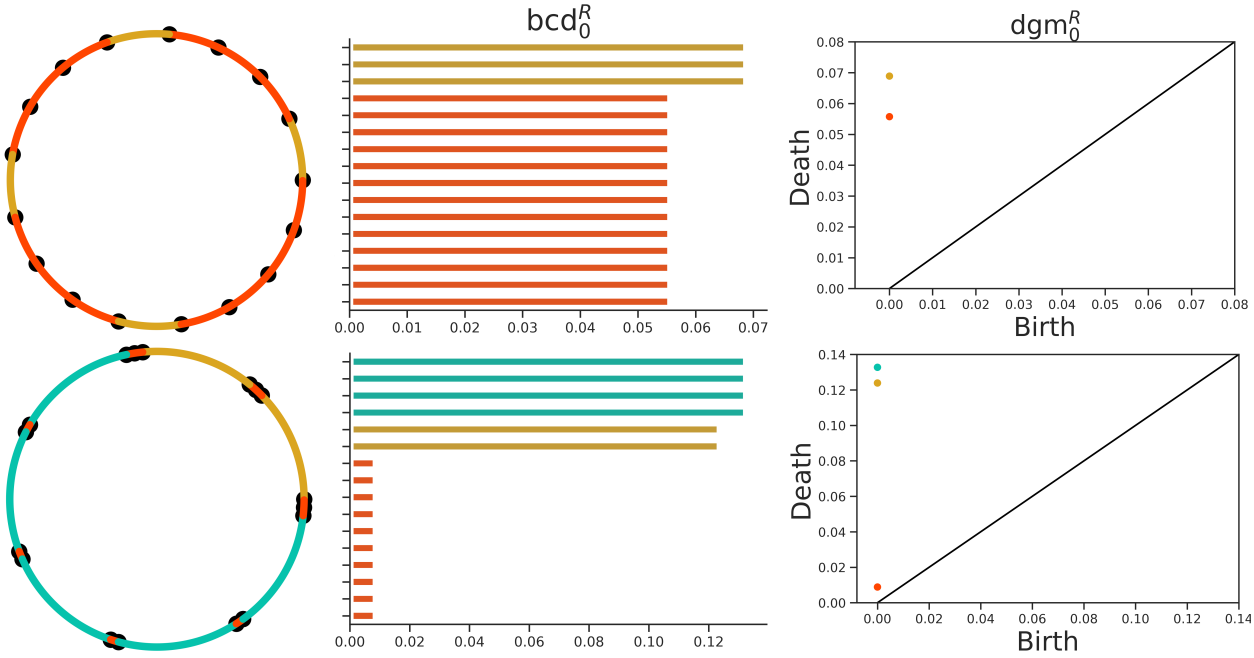

Figure 4.3 We illustrate above how the 0-th dimensional persistent homology can be computed using the Three Gap Theorem. At $\epsilon = 0$ all of the points in $(S_{\omega,T}, \bar{d})$ count as a basis in $H_0(R_\epsilon(S_{\omega,T}, \bar{d}); \mathbb{F})$ (birth time). At $\epsilon = \delta_A$ is the first instance points get connected, in fact the three possible gaps are the only time when components are lost (death time). Top row: The set $S_{\pi-1,17}$ is illustrated with the two gaps it creates. These can be traced in the barcodes and persistent diagram as shown. Bottow row: The set $S_{\sqrt{5},17}$ creates three gaps. Due to clustering, it is a poor covering of the circle. We note $d_2(\pi - 1, \sqrt{5}) = 0.094$.

Theorem 4.2.1. *Let $T \in \mathbb{N}$ and $\omega \in \mathbb{R}\backslash\mathbb{Q}$ with continued fraction $[a_1, a_2, a_3, \cdots]$ and i-th convergent $\frac{p_i}{q_i}$. We assume there are three different intervals generated by $S_{\omega,T}$ and that $\delta_C < 1/2$. If $k \geq 0$ is the unique integer for which*

$$q_k + q_{k-1} \leq T < q_k + q_{k+1},$$

$D_i = q_i\omega - p_i$, and r,s are the unique integers satisfying

$$T = rq_k + q_{k-1} + s, \quad 1 \le r \le a_{k+1}, \quad 0 \le s \le q_k - 1,$$

then $H_0(R_\epsilon(S_{\omega,T}, \bar{d}); \mathbb{F}) =$

$$\begin{cases} \mathbb{F}^{T+1} & 0 \le \epsilon < |D_k| \\ \mathbb{F}^{q_k} & |D_k| \le \epsilon < |D_{k+1}| + (a_{k+1} - r)|D_k| \\ \mathbb{F}^{q_k - s - 1} & |D_{k+1}| + (a_{k+1} - r)|D_k| \le \epsilon \\ & < |D_{k+1}| + (a_{k+1} - r + 1)|D_k| \\ \mathbb{F} & |D_{k+1}| + (a_{k+1} - r + 1)|D_k| \le \epsilon \end{cases}.$$

We also compute $\mathrm{dgm}_1^R(S_{\omega,T}, \bar{d})$ using information from the Three Gap Theorem. We assume $S_{\omega,T}$ has three different gaps and the notation from before. The case in which it has only two gaps can be handle analogously.

Theorem 4.2.2. *Suppose $\delta_C < 1/3$. Let Γ be the set containing the pairs (x, y), $x, y \in S_{\omega,T}$ and $x < y$, for which there exists a $z \in ([0, x) \cup (y, 1)) \cap S_{\omega,T}$ such that $1 - \bar{d}(x, y) \le 2\bar{d}(y, z) \le 2\bar{d}(x, y)$. If*

$$\lambda = \min\{\bar{d}(x, y) |\ (x, y) \in \Gamma\},$$

then $H_1(R_\epsilon(S_{\omega,T}, \bar{d}); \mathbb{F}) =$

$$\begin{cases} \mathbb{F} & |D_{k+1}| + (a_{k+1} - r + 1)|D_k| \le \epsilon < \lambda \\ \emptyset & else \end{cases}.$$

Proof. Let $\{x_i\}_{i=0}^T$ denote the points of $S_{\omega,T}$ in ascending order. Consider the 1-simplex $\sigma = \sum_{i=0}^T \{x_i, x_{i\oplus 1}\}$ where $\oplus$ is mod(T+1) addition. We note $\partial(\sigma) = 0$ and $\sigma \in R_\epsilon(S_{\omega,T}, \bar{d})$ if and only

if $\epsilon \geq \delta_C = |D_{k+1}| + (a_{k+1} - r + 1)|D_k|$ by the Three Gap Theorem. Furthermore, any 1-simplex σ_0 for which $\partial(\sigma_0) = 0$ is homologous to σ.

Now we demonstrate there are no 2-simplex $\tau \in R_{\delta_C}(S_{\omega,T}, \bar{d})$ such that $\partial(\tau) = \sigma$. We assume this to be true and arrive at a contradiction. By reindexing and translating, we can assume $\bar{d}(0, x_1) = \delta_C$. By assumption, there needs to exist a $\{0, x_1, x_i\} \in \tau^2$ for some $i > 1$. If $x_i \leq 1/2$ then $\bar{d}(0, x_i) = \bar{d}(0, x_1) + \bar{d}(x_1, x_i) > \delta_C$ and if $x_i > 1/2$, then $\bar{d}(x_1, x_i) =$

$$\min\{\bar{d}(0, x_1) + \bar{d}(0, x_i), 1 - (\bar{d}(0, x_1) + \bar{d}(0, x_i))\} > 1/3,$$

($\delta_C < 1/3$). Thus, $\{0, x_1, x_i\} \notin \tau^2$ for all $i > 1$, a contradiction.

To conclude the proof, it suffices to show that for $\epsilon \in (\delta_C, \lambda]$ there exists a 2-simplex $\tau \in R_\epsilon(S_{\omega,T}, \bar{d})$ such that $\partial(\tau) = \sigma$ if and only if $\epsilon = \lambda$. We first show the forward direction. Let $(x_{n_1}, x_{n_2}) \in \Gamma$ be such that $\lambda = \bar{d}(x_{n_1}, x_{n_2})$ and x_{n_3} be a point associated with the pair as described in the statement of the theorem. We note $\bar{d}(x_{n_2}, x_{n_3}) \leq \bar{d}(x_{n_1}, x_{n_2}) = \lambda$ and $\bar{d}(x_{n_2 1}, x_{n_3}) \leq 1 - \bar{d}(x_{n_1}, x_{n_2}) - \bar{d}(x_{n_2}, x_{n_3}) \leq \bar{d}(x_{n_2}, x_{n_3}) \leq \lambda$. Thus, $\{x_{n_1}, x_{n_2}, x_{n_3}\} \in R_\lambda(S_{\omega,T}, \bar{d})$. Let

$$\tau_1 = \sum_{n_1 \leq i < n_2 - 1} \{x_i, x_{i+1}, x_{n_2}\}.$$

By keeping track of the index at zero, one can define analogues τ_2, τ_3 corresponding to the pairs (x_{n_2}, x_{n_3}), (x_{n_3}, x_{n_1}), respectively. Let $\tau = \tau_1 + \tau_2 + \tau_3 + \{x_{n_1}, x_{n_2}, x_{n_3}\}$. One can verify $\tau \in R_\lambda(S_{\omega,T}, \bar{d})$ and that $\partial(\tau) = \sigma$ as desired.

For the reverse direction, let $\epsilon \in (\delta_C, \lambda)$. If one assumes the existence of such 2-simplex, say $\tau_0 \in R_\epsilon(S_{\omega,T}, \bar{d})$, one can show this will contradict the minimality of λ by considering $\max\{\bar{d}(x, y) \mid \text{there exists } \{x, y, z\} \in \tau_0^2\}$.

□

4.2.2 Bottleneck Distance

We can apply our result to obtain explicit formulas for the the stability with respect to the bottleneck distance as detailed in Section 2. These results provide a way of obtaining the ϵ_0 and ϵ_1 shown in 3.3.1 without using Ripser or Persim [16, 36]. We present our results following the

notation used in Section 2. Furthermore, we assume there are three gaps and that the biggest one has multiplicity of at least two. We also impose assumptions in the statement for the sake of simplifying the presentation. The proof for the other cases is analogues.

Theorem 4.2.3. *Suppose*

$$x_j = \bar{x}_j$$

for some $j \in \mathbb{N}$ *and*

$$q_{k_j(\alpha)-1} + q_{k_j(\alpha)-2} \leq N < q_{k_j(\alpha)-1} + q_{k_j(\alpha)}.$$

Let r, s *be the unique integers satisfying*

$$N = rq_{k_j(\alpha)-1} + q_{k_j(\alpha)-2} + s, \qquad 1 \leq r \leq a_{k_j(\alpha)}, \quad 0 \leq s \leq q_{k_j(\alpha)-1} - 1.$$

We assume $r < a_{k_j(\alpha)}$, $N - q_{k_j(\alpha)-1} > s$, $\alpha > \bar{\alpha}$, *and* $k_j(\alpha)$ *is even. Let* $D_i(x) = |q_i x - p_i|$,

$$K_1(x) = D_{k_j(\alpha)}(x) + (a_k - r)D_{k_j(\alpha)-1}(x), \quad K_2(x) = D_{k_j(\alpha)}(x) + (a_k - r + 1)D_{k_j(\alpha)-1}(x)$$

and

$$\Delta_1 = (\alpha - \bar{\alpha})(q_{k_j(\alpha)} - q_{k_j(\alpha)-1}(a_{k_j(\alpha)} - r)), \quad \Delta_2 = (\alpha - \bar{\alpha})(q_{k_j(\alpha)} - q_{k_j(\alpha)-1}(a_{k_j(\alpha)} - r + 1)).$$

Then,

$$d_B(dgm_0^R(S_{\alpha,N}), dgm_0^R(S_{\bar{\alpha},N})) = \max\{\min\{\Delta_1, \frac{K_1(\bar{\alpha})}{2}\}, \min\{\Delta_2, \frac{K_2(\bar{\alpha})}{2}\}\}.$$

Proof. For $1 \leq i \leq 3$, let δ_i and $\bar{\delta}_i$ denote the length of the three gaps in increasing size of $S_{\alpha,N}$ and $S_{\bar{\alpha},N}$ respectively. The assumptions imply $\bar{\delta}_3 > \delta_3$, $\bar{\delta}_2 > \delta_2$, and that we can match each point $(0, \delta_i)$ with a $(0, \bar{\delta}_i)$. This leads to a $(\bar{\delta}_2 - \delta_2)$-matching since

$$\delta_1 - \bar{\delta}_1 = (\alpha - \bar{\alpha})q_{k_j(\alpha)-1} \leq (\alpha - \bar{\alpha})(q_{k_j(\alpha)-2} + q_{k_j(\alpha)-1}r) = \delta_2 - \bar{\delta}_2$$

and $(\bar{\delta}_3 - \delta_3) = (\bar{\delta}_2 - \delta_2) - (\delta_1 - \bar{\delta}_1)$. Now, we argue matching $(0, \bar{\delta}_3)$ with $(0, \delta_2)$ or $(0, \delta_1)$ leads to a worse matching. Indeed, this follows by noting

$$\bar{\delta}_3 - \delta_2 = (\bar{\delta}_2 - \delta_2) + \bar{\delta}_1$$

and $\bar{\delta}_3 - \delta_1 > \bar{\delta}_3 - \delta_2$. Thus, the only possibly better matches can be obtain from matching to $(0, \delta_3)$ or to $(\frac{\bar{\delta}_3}{2}, \frac{\bar{\delta}_3}{2})$,. The best matching obtained from the latter scenario is a $\frac{\bar{\delta}_3}{2}$-matching since $\bar{\delta}_3 > \delta_3$. For the former case, the situation can only improve by matching $(0, \bar{\delta}_2)$ with $(\frac{\bar{\delta}_2}{2}, \frac{\bar{\delta}_2}{2})$ or with $(0, \delta_1)$, but

$$\bar{\delta}_2 - \delta_1 = (\bar{\delta}_2 - \delta_2) + (\delta_2 - \delta_1).$$

We conclude the best matching is a r-matching, where

$$r = \max\{\min\{(\bar{\delta}_2 - \delta_2), \frac{\bar{\delta}_2}{2}\}, \min\{(\bar{\delta}_3 - \delta_3), \frac{\bar{\delta}_3}{2}\}\}.$$

The result now follows by substituting the expressions of the gaps using The Three Gap Theorem and noting that for $0 \leq i \leq k_j(\alpha)$

$$\alpha > \frac{p_i}{q_i} \quad \text{iff} \quad \bar{\alpha} > \frac{p_i}{q_i}.$$

□

Similarly, we can apply the results of The Three Gap Theorem to obtain the bottleneck distance in the case of the 1-st dimensional persistence diagrams. We make the assumptions in the previous results and use the notation λ_α to denote the λ from Theorem 4.2.2 corresponding to the sampling parameter α. As before, the assumptions made are to simplify the presentation of the statement.

Theorem 4.2.4. *Let*

$$T(x) = \frac{1}{2}(\lambda_x - K_2(x)),$$

then

$$d_B(dgm_1^R(S_{a,N}), dgm_1^R(S_{\bar{a},N})) = \min\{\max\{\Delta_2, |\lambda_a - \lambda_{\bar{a}}|\}, \max\{T(a), T(\bar{a})\}\}.$$

4.3 Approximation method

We present our method in the next theorem in which we denote by σ_{min} and σ_{max} the smallest and biggest, respectively, eigenvalue of A. We also denote by d_{GH} the Gromov-Hausdorff distance computed in $(\mathbb{C}^N, d_\infty)$, where d_∞ denotes the supremum metric.

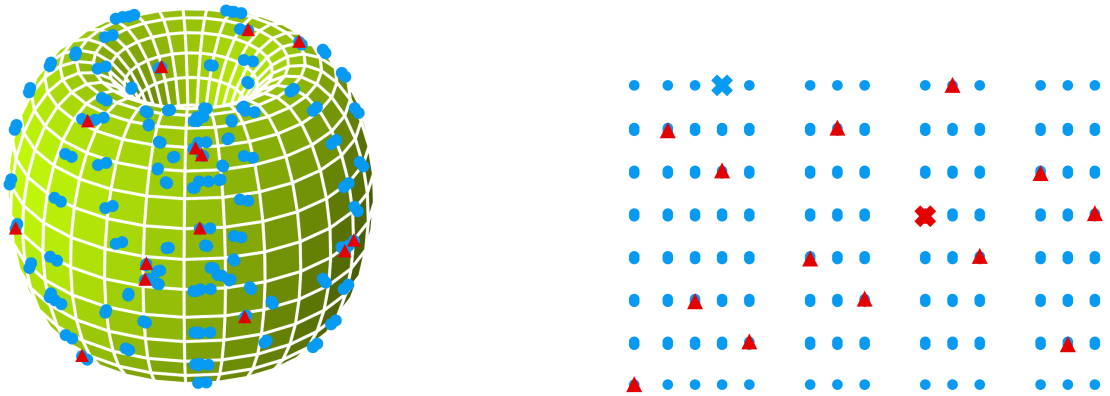

Figure 4.4 Depiction of $\phi(13)$ (red triangles) and $G(13)$ (blue dots) in the case of two incommensurate frequencies. Left: Points are in the torus. Right: Points are plotted using the rectangular representation of the torus. The pair marked with an x achieve the Hausdorff distance between the two sets.

Theorem 4.3.1. *Let*

$$f(t) = \sum_{j=1}^{M} c_j e^{i\omega_j t}, \qquad c_j \in \mathbb{C},\ \omega_j \in \mathbb{R}.$$

Suppose $N \leq M$ is the maximum number of incommensurate frequencies, say $\{\omega_l\}_{l=1}^{N}$. For $N < l \leq M$ and $\bar{t} \in \mathbb{N}^N$ let

$$\bar{\omega}_l(\bar{t}) = \sum_{j=1}^{N} \bar{t}_j \lambda_j^l \omega_j,$$

where $\lambda_j^i \in \mathbb{Q}$ and $\bar{\omega}_l((1,1,\ldots,1)) = \omega_l$. Given $T \in \mathbb{N}$ and $\bar{c}_i = \sqrt{d+1}\, c_i$ we define $\phi(T) =$

$$\{(\bar{c}_1 e^{i\omega_1 t}, \ldots, \bar{c}_M e^{i\omega_M t})^\intercal\}_{0 \leq t \leq T},$$

$G_T =$

$$\{(\bar{c}_1 e^{i\omega_1 \bar{t}_1}, \ldots, \bar{c}_{N+1} e^{i\bar{\omega}_{N+1}(\bar{t})}, \ldots, \bar{c}_M e^{i\bar{\omega}_M(\bar{t})})^\intercal\}_{0 \leq \bar{t}_i \leq T},$$

$k = \max\{\sigma_{min}^{-1}, \sigma_{max}\sqrt{M}\}$ and $\lambda = d_{GH}(\phi(T), G(T'))$, where $T' \leq T$. If $(a_1, b_1) \in dgm_j^R(G(T'), d_\infty)$ satisfies

$$\frac{b_1 - 2\lambda}{a_1 + 2\lambda} > \max\{k^2, 1\},$$

then there exists a unique $(a_2, b_2) \in dgm_j^R(\{SW_{d,\tau} f(t)\}_{t=0}^{T}, d_2)$ satisfying

$$\max\left\{0, \frac{b_1 - 2\lambda}{k}\right\} \leq\ b_2\ \leq k\ (b_1 + 2\lambda)$$

$$\max\left\{0, \frac{a_1 - 2\lambda}{k}\right\} \leq\ a_2\ \leq k\ (a_1 + 2\lambda).$$

Proof. Our first task will be to apply the Stability Theorem [37] to relate (a_1, b_1) with a unique $(a_0, b_0) \in \mathrm{dgm}_j^R(\phi(T), d_\infty)$. In turn, by using the Isometry Theorem [38] we will match (a_0, b_0) with a unique $(a_2, b_2) \in \mathrm{dgm}_j^R(\{SW_{d,\tau}f(t)\}_{t=0}^T, d_2)$. We conclude the result by keeping track of the relations throughout.

By Theorem 2.1.14, if $b_1 - a_1 > 4\lambda$ then there exists a unique $(a_0, b_0) \in \mathrm{dgm}_j^R(\phi(T), d_\infty)$ such that $|b_1 - b_0| < 2\lambda$ and $|a_1 - a_0| < 2\lambda$. To relate (a_0, b_0) to a $(a_2, b_2) \in \mathrm{dgm}_j^R(\{SW_{d,\tau}f(t)\}_{t=0}^T, d_2)$ we note

$$\sigma_{min} d_\infty(v_{t_1}, v_{t_2}) \leq d_2(Av_{t_1}, Av_{t_2})$$

and

$$d_2(Av_{t_1}, Av_{t_2}) \leq \sqrt{M}\sigma_{max} d_\infty(v_{t_1}, v_{t_2}),$$

where $SW_{d,\tau}f(t) = Av_t$. This allow us to find an interleaving between the two persistent modules using a logarithmic scale, namely a $ln(k)$ interleaving. Thus, by the Isometry Theorem we can say that if $\frac{b_0}{a_0} > k^2$ then there exists a unique $(a_2, b_2) \in \mathrm{dgm}_j^R(\{SW_{d,\tau}f(t)\}_{t=0}^T, d_2)$ such that

$$\frac{1}{k} < \frac{\max\{b_0, b_2\}}{\min\{b_0, b_2\}}, \frac{\max\{a_0, a_2\}}{\min\{a_0, a_2\}} < k.$$

Putting it all together, we can say that if

$$\frac{b_1 - 2\lambda}{a_1 + 2\lambda} > \max\{k^2, 1\}$$

then there exist a unique $(a_0, b_0) \in \mathrm{dgm}_j^R(\phi(T), d_\infty)$ such that $a_0 < a_1 + 2\lambda$ and $b_0 > b_1 - 2\lambda$. Thus,

$$\frac{b_0}{a_0} > \frac{b_1 - 2\lambda}{a_1 + 2\lambda} > k^2$$

implying there exists a unique

$$(a_2, b_2) \in \mathrm{dgm}_j^R(\{SW_{d,\tau}f(t)\}_{t=0}^T, d_2)$$

such that, say if $b_0 = \max\{b_0, b_2\}$,

$$\frac{1}{k} < \frac{b_0}{b_2} < k$$

and thus

$$\frac{b_1 - 2\lambda}{k} < b_2 < k(b_1 + 2\lambda).$$

The same result holds when $b_2 = \max\{b_0, b_2\}$. One can show an analogues inequality for the birth time as well. The result follows.

□

We note that for the case $N = M$, $\mathrm{dgm}_j^R(G(T'), d_\infty)$ can be computed for $j = 1, 2$ using our main results. This is achieved by using the persistent Künneth formula [14]. We are able to leverage our results since

$$d_2(c_l e^{i\omega_l t_1}, c_l e^{i\omega_l t_2}) = 2|c_l|\sin(\pi \bar{d}([\omega_l' t_1], [\omega_l' t_2])),$$

for $t_1, t_2 \in \mathbb{N}$ and $w_l' = \frac{\omega_l}{2\pi}$. Furthermore, by noting

$$d_2(c_l e^{i\omega_l t_1}, c_l e^{i\omega_l t_2}) = d_2(c_l e^{-i\omega_l t_1}, c_l e^{-i\omega_l t_2})$$

we can obtain the following result:

Theorem 4.3.2. *Let*

$$f(t) = \sum_{j=1}^{N} c_j(e^{i\omega_j t} + e^{-i\omega_j t}), \qquad c_j \in \mathbb{C},\ \omega_j \in \mathbb{R},$$

where $\{\omega_j\}_{j=1}^N$ *is incommensurate. For* $a, b, s \in \mathbb{R}$, *let* $\bar{a} = 2\ \sin(\pi a)$, $\omega_l' = \frac{\omega_l}{2\pi}$, *and for* $I = [a, b)$ *we let* $\bar{I} = [\bar{a}, \bar{b})$ *and write* sI *to denote* $[sa, sb)$. *Given* $T \in \mathbb{N}$ *and* $\bar{c}_l = \sqrt{(4N+2)|c_l|^2}$, *we define* $\phi(T) =$

$$\{(\bar{c}_1 e^{i\omega_1 t}, \ldots, \bar{c}_N e^{i\omega_N t})^\intercal\}_{0 \le t \le T},$$

$G_T =$

$$\{(\bar{c}_1 e^{i\omega_1 \bar{t}_1}, \ldots, \bar{c}_N e^{i\omega_N \bar{t}_N})^\intercal\}_{0 \le \bar{t}_i \le T},$$

$k = \max\{\sigma_{min}^{-1}, \sigma_{max}\sqrt{N}\}$ *and* $\lambda = d_{GH}(\phi(T), G(T'))$, *where* $T' \le T$. *If* $[a_1, b_1) \in$

$$\bigcup_{\sum_l r_l = j} \left\{\bar{c}_1 \bar{I}_1 \cap \cdots \cap \bar{c}_N \bar{I}_N \mid I_l \in bcd_{r_l}^R(S_{\omega_l', T'}, \bar{d})\right\},$$

satisfies

$$\frac{b_1 - 2\lambda}{a_1 + 2\lambda} > \max\{k^2, 1\},$$

then there exists a unique $(a_2, b_2) \in dgm_j^R(\{SW_{d,\tau} f(t)\}_{t=0}^T, d_2)$ *satisfying*

$$\max\left\{0, \frac{b_1 - 2\lambda}{k}\right\} \leq \ b_2 \ \leq k\ (b_1 + 2\lambda)$$

$$\max\left\{0, \frac{a_1 - 2\lambda}{k}\right\} \leq \ a_2 \ \leq k\ (a_1 + 2\lambda).$$

We note that our results allow us to approximate (a_2, b_2) with an error bound. Indeed, when the right conditions are met, the theorem guarantees the point to lie inside of the rectangle with the vertices shown below:

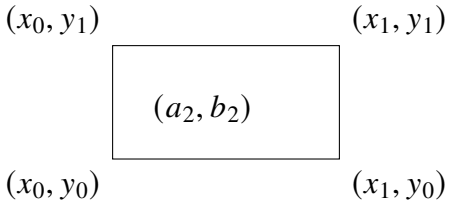

where $x_0 = \max\{0, \frac{a_1 - 2\lambda}{k}\}$, $x_1 = k(a_1 + 2\lambda)$, $y_0 = \max\{0, \frac{b_1 - 2\lambda}{k}\}$, and $y_1 = k(b_1 + 2\lambda)$. Thus, our approximation (a_1, b_1) provides the rectangle as a confidence region.

4.3.1 Example

We apply our method to the function $f(t) = \frac{1}{\sqrt{2}} e^{i\sqrt{5}t} + \frac{1}{\sqrt{2}} e^{i\sqrt{3}t}$. By appropriate choice of parameters, $d = 1$, and $\tau = \frac{\pi}{\sqrt{5} - \sqrt{3}}$, we can make the matrix A be orthogonal. We also compare our method to two other approximations of $SW(n)$: landmarks $\mathrm{SW}_L(n)$ and landmarks for the Künneth formula $\mathrm{K}_L(n)$, where n is the number of samples used [14].

4.4 Concluding remarks

In this chapter we introduced the approximation method 3G. It approximates the persistence diagram from SW. We were able to compute much faster results by using frequency information thanks to the Three Gap Theorem. We then combined results obtained from single frequencies to treat the quasiperiodic case using the Künneth formula in persistent homology. Under the right conditions, our approximation can include error bounds obtained from the Isometry Theorem

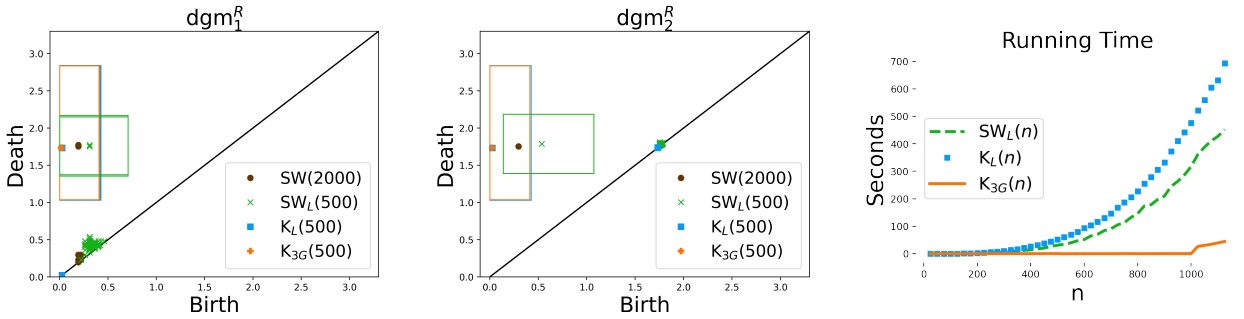

Figure 4.5 Diagrams from example 4.1. We also illustrate the running time it takes when using Ripser [16] for SW and K_L. Our code is denoted as K_{3G}; we note Ripser is not used at any step in our code.

and the Stability Theorem. We hope our approach contributes to the use of the sliding window embedding technique on large data sets.

CHAPTER 5

APPLICATIONS

In this section we will apply our pipeline, 3G, to the following examples: Synthetic tremor signals, in the nonlinear tuned vibration absorber it is an indicator of safe or unsafe operations [39]. Neuroscience, where quasiperiodicity is associated to task-specific functions in certain brain areas [40]. Celestial mechanics, where quasiperiodicity translates to nice trajectories for a mission [41]. We contribute to this fields by providing a faster alternative (see Figure 4.5 and Table 5.1) to analyze the reconstructed signal of potential quasiperiodic signals.

5.1 Methodology

We work with dynamical systems for which Φ is known. In particular, we work with ordinary differential equations associated to the system. These equations dictate the evolution of the system across time. To imitate an observation of the system, we use the solutions to create a time series signal f. We reconstruct the system by then computing the sliding window point cloud $\{SW_{d,\tau}f(\epsilon t)\}_{t=0}^{T}$, where ϵ is chosen following the Nyquist-Shannon sampling theorem [42]. The framework detailed in [5] provides a way of selecting d and τ and approximate $\mathrm{dgm}_j^R(\{SW_{d,\tau}f(\epsilon t)\}_{t=0}^{T}, d_2)$ with $\mathrm{dgm}_j^R(\{SW_{d,\tau}S_1f(\epsilon t)\}_{t=0}^{T}, d_2)$. Since S_1f is a sum of the form shown in 4.3, we can apply our results to approximate the latter and as a result get close to the former. Indeed, in the examples we consider

$$S_1f(\epsilon t) = \sum_{j=1}^{2} c_j(e^{i\epsilon\omega_j t} + e^{-i\epsilon\omega_j t}).$$

Thus, 3G can be used to approximate $\mathrm{dgm}_j^R(\{SW_{d,\tau}S_1f(\epsilon t)\}_{t=0}^{T}, d_2)$ with a known error bound as detailed in 4.3.

5.2 Results

We consider systems with known quasiperiodic behavior. Specifically, they are systems with two incommensurate frequencies. Hence, the sliding window point cloud, $\{SW_{d,\tau}f(\epsilon t)\}_{t=0}^{T}$, samples a 2-torus. We label its corresponding persisetence diagrams by $SW(T)$ (shown in brown dots). Similarly, we denote by $SW_{S_1}(T)$ the ones corresponding to $S_1(f)$ (shown in blue squares). The

approximation obtained from $3G$ is labeled as $K_{3G}(T)$ (shown in orange crosses).

5.2.1 Double Gyre

The driven Double Gyre system provides a model for patterns occurring in geophysical flows [43]. A topological approach to it has shown great success. Indeed, as is shown in [44] there are multiple topological classifications that can be observed in the system which represents the motion of a fluid particle. In this work they noted the motion of fluid can be sparse, meaning some initial conditions will imply a particle will be contained in a small region. Indeed, different initial conditions have shown trajectories with a topology of a standard strip, five-handle structure with a torsion, torus and a möbius strip. This result was achieved by calculating homologies in a branched manifold while keeping track of the orientability chains which allowed for the identification of the branches and the localization of twists or torsions. This approach is called Branched Manifold analysis through Homologies (BraMAH). At its core, it follows the principle of reconstructing a dynamical system from a time series. Yet the details at each step are completely different to SW.

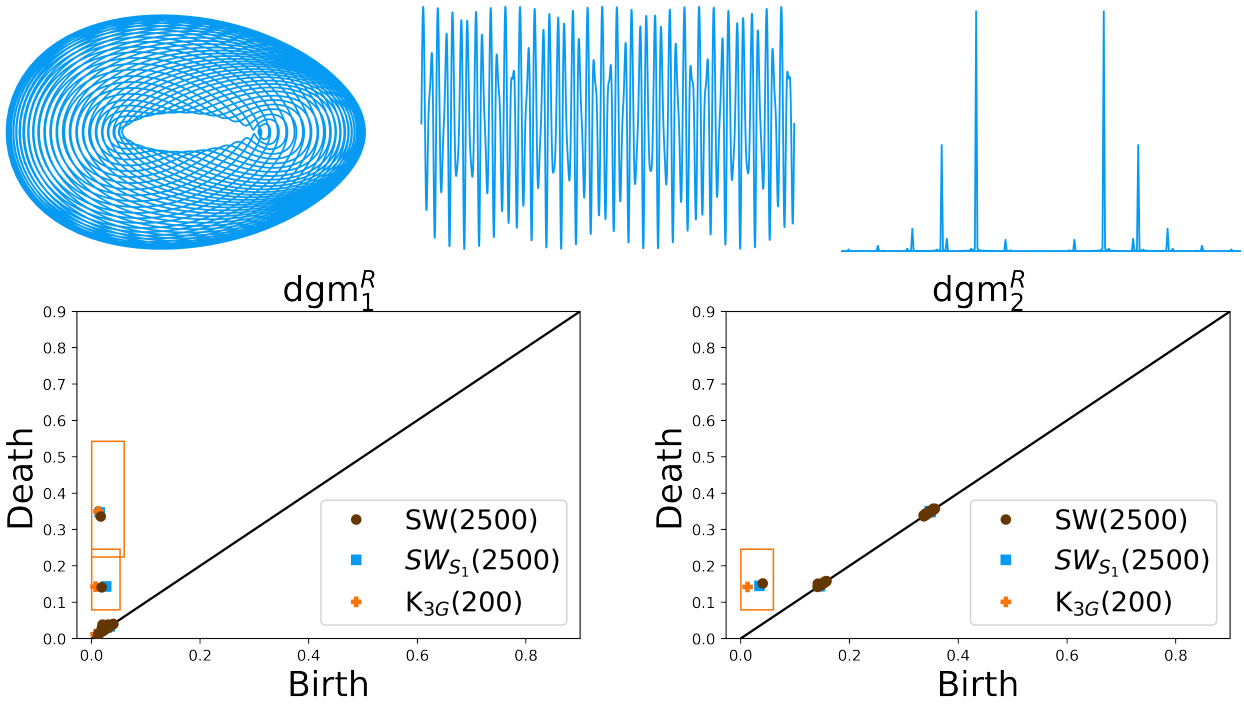

Figure 5.1 Top row: Phase space of the driven Double Gyre system starting at x_0. The solution $x_1(t)$ we used for SW is plotted in the middle followed by its fast fourier transform. Bottom row: Corresponding diagrams.

Nevertheless, for the corresponding initial conditions, we independently corroborated the presence of a torus, i.e. quasiperiodicity in the motion of the fluid particle, see Figure 5.1. This highlight the robustness offered by a topological approach to dynamical systems.

Concretely, the driven Double Gyre is given by the equation $\dot{x} = (-\frac{\partial \psi}{\partial x_2}, \frac{\partial \psi}{\partial x_1})$ where

$$\psi(x_1, x_2, t) = A \sin(\pi g(x_1, t)) \sin(\pi x_2)$$

with

$$g(x_1, t) = \eta \sin(\lambda t)(x_1^2 - 2x_1) + x_1,$$

and parameter values $A, \mu = 0.1$ and $\lambda = \pi/5$. The system has a toroidal attractor for the initial condition $x_0 = (0.5, 0.625)$ [44]. We solve the system using $dt = 0.1$ up to $t = 800$. Furthermore, SW is done using $f = x_1,\ d = 4,\ \tau = 119.03,$ and $\epsilon = 0.1$.

5.2.2 Torus in $\mathbb{R}^4$

We move on to consider the torus in rectangular coordinates. It is given by the set of equations:

$$\dot{x} = -y + x(1 - \sqrt{x^2 + y^2}), \qquad \dot{y} = x + y(1 - \sqrt{x^2 + y^2}),$$
$$\dot{z} = -kr + z(4 - \sqrt{z^2 + r^2}), \qquad \dot{r} = kz + r(4 - \sqrt{z^2 + r^2}).$$

When k is irrational, the solutions span a torus [45]. We considered the case $k = \sqrt{2}$ with initial condition $(x_0, y_0, z_0, r_0) = (1, 0, 4, 0)$. We solve the system with $dt = 0.1$ up to $t = 800$. SW is

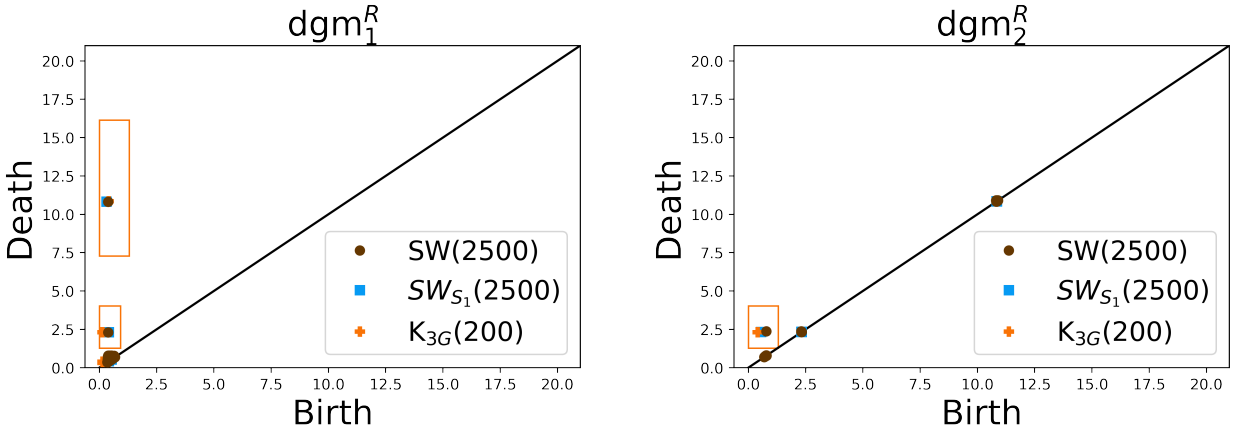

Figure 5.2 Diagrams obtained for the torus in $\mathbb{R}^4$.

done using $f = x + z,\ d = 4,\ \tau = 87.56,$ and $\epsilon = 0.1$, see Figure 5.2.

5.2.3 Pendulum Attached to a Sliding Block

We now consider a particular type of tune mass damper (TMD). TMD is a device used to suppress vibration by moving a mass attached to the main structure through springs and dampers [22]. This model has been successfully used to dampen the effect of long duration earthquake ground motions [21]. Indeed, one can consider the main structure being a skyscraper and the incoming wave being generated by the earthquake. Thus, a better understanding of this system translates to earthquake-resistant technologies.

We consider the case of a pendulum attached to a sliding block, see Figure 5.3. It was shown to exhibit quasiperiodicity in [22]. The governing equations are:

$$\ddot{x} + \alpha^2 x - \bar{\epsilon} g\theta - \bar{\epsilon} L\dot{\theta}^2\theta = 0$$

$$\ddot{\theta} + (1+\bar{\epsilon})\beta^2\theta - \bar{\epsilon} h\alpha^2 x + \bar{\epsilon}\dot{\theta}^2\theta = 0$$

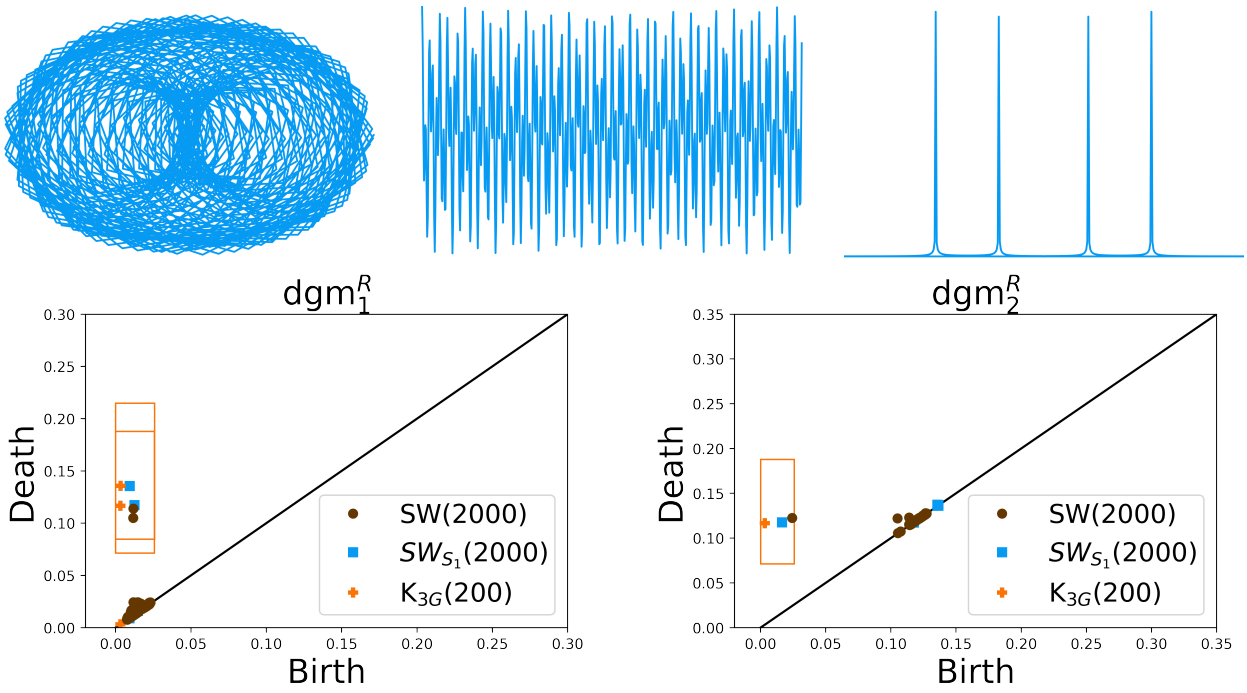

Figure 5.3 Top row: Plot of $(x, \dot{x})$ from the pendulum attached to a sliding block. The solution $x(t)$ we used for SW is plotted in the middle followed by its fast fourier transform. Bottom row: Persistence diagrams.

in which

$$\bar{\epsilon} = \frac{m}{M}, \quad \alpha = \sqrt{\frac{k}{M}}, \quad \beta = \sqrt{\frac{g}{L}}, h = \frac{1}{\bar{\epsilon}L},$$

and g is the acceleration of gravity. The parameter values are $m = 0.5,\ M = 1,\ L = 1,$ and $k = 5$. We solve the system with initial condition $(x_0, \dot{x}_0, \theta_0, \dot{\theta}_0) = (0.1, 0, -0.1, 0)$ and $dt = 0.27$ up to $t = 540$. SW is done using $f = x,\ d = 4,\ \tau = 108.05,$ and $\epsilon = 0.027$.

5.2.4 Generalized Wilson-Cowan Equations

We consider a generalized version of the Wilson-Cowan equations shown in Example 2.2.3. Traditionally, these equations are derived via a time-coarse graining technique that averages the response. They also restrict to a weak Gamma distribution of time delays. The extended model has been treated in [40], it is given by

$$\dot{u}(t) = -u(t) + f_1\Big(\theta_u + \int_{-\infty}^{t} h(t-s)(au(s) + bv(s))\, ds\Big),$$

$$\dot{v}(t) = -v(t) + f_2\Big(\theta_v + \int_{-\infty}^{t} h(t-s)(cu(s) + dv(s))\, ds\Big),$$

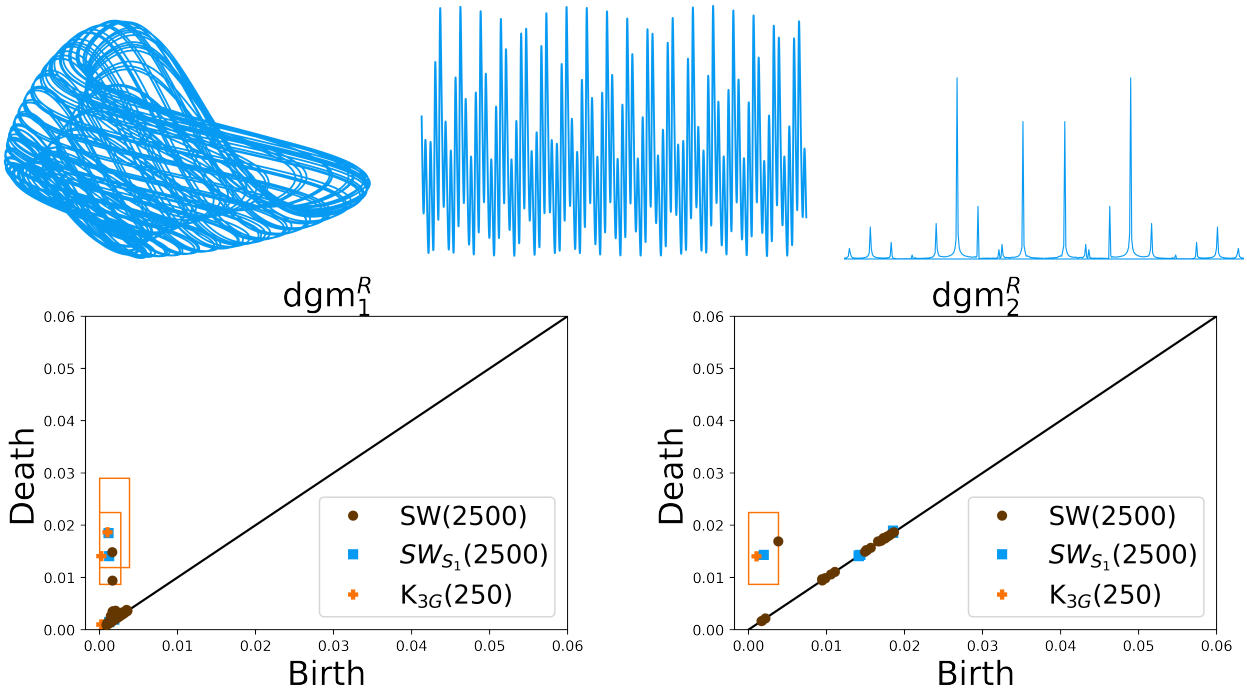

Figure 5.4 Top row: Plot of (u, v) from the generalized Wilson-Cowan equations. The solution $u(t)$ we used for SW is plotted in the middle followed by its fast fourier transform. Bottom row: Persistence diagrams.

where $u(t)$ and $v(t)$ model the firing activity in two neuronal populations, a,b,c,d are the connection weights and θ_u, θ_v are background drives. The activation functions f_1, f_2 are smooth and increasing on the real line. The authors considered three types of delay kernel $h : [0, \infty) \to [0, \infty)$, namely, weak Gamma, strong Gamma, and Dirac kernel. Their analysis indicates a kernel is preferable based on the function of the model populations.

One can readily verify this system recovers the Wilson-Cowan equations in the case of a weak Gamma kernel. We consider the case of a Dirac kernel, see Figure 5.4. This system has been shown to exhibit quasiperiodicity [40, 46]. Furthermore, it has applications to the subthalamic nucleus - globus pallidus network involved in Parkinson's Disease (guided by anatomical and electrophysiological research) [47]. The system of interest becomes

$$\dot{u}(t) = -u(t) + f_1(\theta_u + au(t - \tau_1) + bv(t - \tau_2)),$$

$$\dot{v}(t) = -v(t) + f_2(\theta_v + cu(t - \tau_2) + dv(t - \tau_1))$$

where

$$f_1(x) = f_2(x) = \frac{1}{1 + e^{-\delta x}}.$$

The parameter values are $\theta_u = 0.1,\ \theta_v = 0.2,\ \tau_1 = \tau_2 = 0.152,\ a = d = -19,\ b = c = 10$, and $\delta = 10$. We solve the system with initial conditions $(u_0, v_0) = (0.05, 0.05)$ and $dt = 0.001$ up to $t = 50$. SW is done using $f = u,\ d = 4,\ \tau = 1.712$, and $\epsilon = 0.01$.

5.2.5 Electromagnetic Radiation on a Wilson Neuron Model

Wilson introduced a simplified model for a neocortical neuron by making assumptions on the Hodgkin-Huxley model [48]. The biophysics of these neurons is governed by the interplay of about a dozen ion currents. His model showed the need of only four ion currents to accurately replicate known spiking behavior. We analyze an extension of his model that incorporates the presence of electromagnetic radiation (EMR).

Commonplace presence of electronic devices introduces EMR exposure to neurons. The effects EMR has was imitated with the presence of a flux-controlled memristor in [49]. Their proposed model was shown to exhibit quasiperiodicity and their results were successfully replicated using

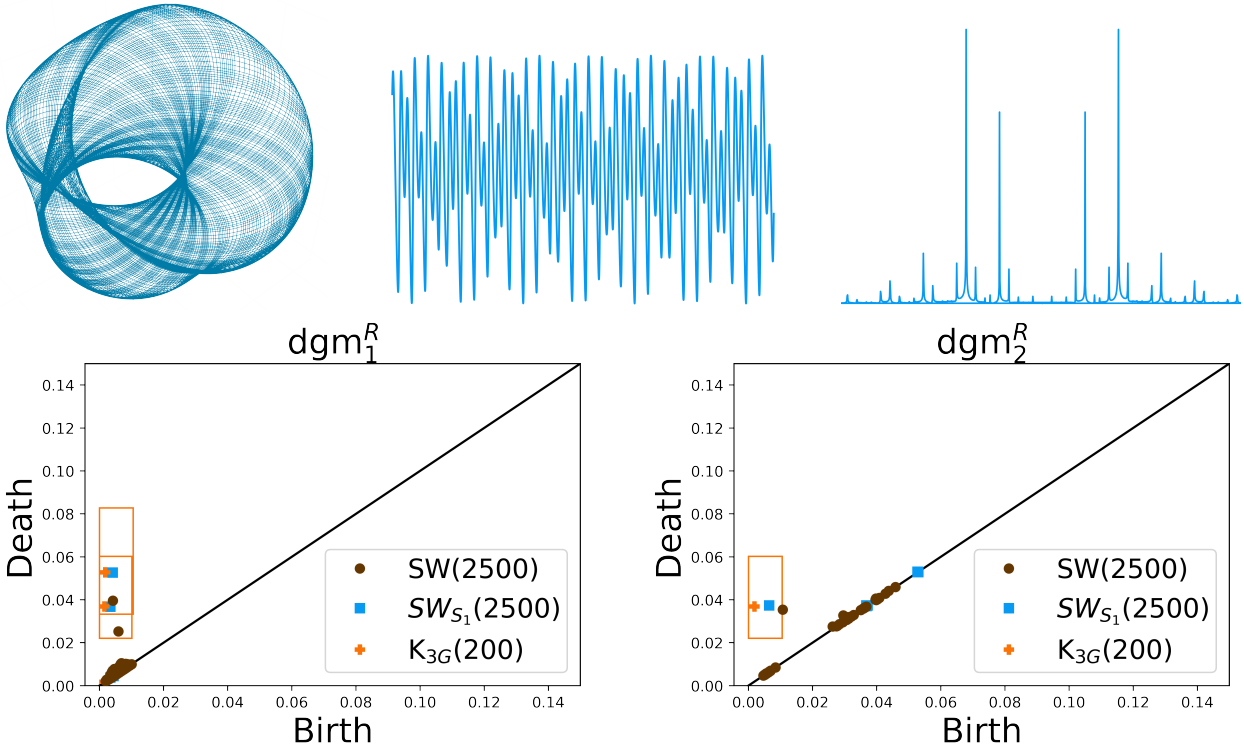

Figure 5.5 Top row: Depiction of the phase space in (v, r, ϕ). The solution $r(t)$ we used for SW is plotted in the middle followed by its fast fourier transform. Bottom row: Persistence diagrams.

a micro-controller unit based hardware platform. Their mathematical model describe membrane potential v, recovery variable r, and inner state of the memristor ϕ

$$C_m \frac{dv}{dt} = -m_\infty(v)(v - E_{Na}) - g_K r(v - E_K) + I_{ext} - k_1 W(\phi)v,$$

$$\frac{dr}{dt} = \frac{1}{\tau_r}(-r + r_\infty(v)), \qquad \frac{d\phi}{dt} = v - k_2\phi + \phi_{ext}$$

where

$$m_\infty(v) = 17.8 + 47.6v + 33.8v^2$$

and

$$r_\infty(v) = 1.24 + 3.7v + 3.2v^2.$$

We use typical model parameters for the membrane capacitor, $C_m = 1$, reverse potential for sodium and potassium, $E_{Na} = 0.5$ and $E_K = -0.95$, respectively, maximal conductance of potassium, $g_K = 26$, potassium ion channel activation time constant, $\tau_r = 5$, and external stimulus current $I_{ext} = 1$ [50]. The EMR external contribution is given by $\phi_{ext} = A\sin(2\pi Ft)$, the terms $k_1 W(\phi)v$

and $k_2\phi$ denote the induction current caused by variation of magnetic flux and the leakage of magnetic flux. The memductance of the memristor is given by $W(\phi) = a - b\tanh\phi$ [51]. The remaining parameter values are $a = 1$, $b = 3$, $k_1 = 1.2$, $k_2 = 0.5$, $A = 0.35$, and $F = 0.22$. We solve the system using the initial conditions $(v_0, r_0, \phi_0) = (0, 0, 0)$ and $dt = 0.01$ up to $t = 500$. SW was done with $f = r$, $d = 4$, $\tau = 72.21$, and $\epsilon = 0.07$, see Figure 5.5.

5.2.6 Competitive Threshold-Linear Network

Threshold-linear networks (TLNs) provide an accessible model acting under the presence of a threshold nonlinearity [ref]. It provides a refinement to linear approximations of networks. The latter can be conceptualized as a directed graph, G, in which nodes interact. The TLN model can be described by the equations

$$\frac{dx_i}{dt} = -x_i + \left[\sum_{j=1}^{n} W_{ij}x_j + b_i\right]_+$$

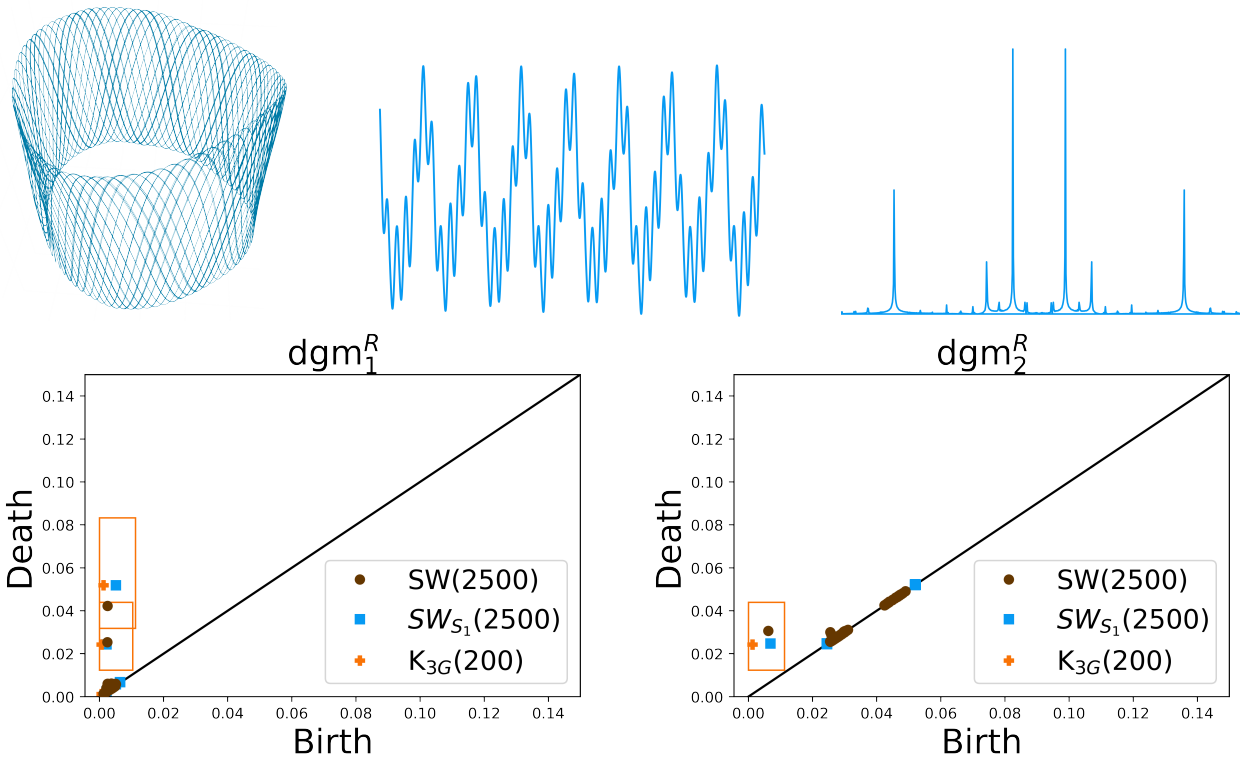

Figure 5.6 Top row: PCA representation in three dimensions of the competitive TLN solutions. The solution $x_4(t)$ we used for SW is plotted in the middle followed by its fast fourier transform. Bottom row: Persistence diagrams.

where $i = 1, \ldots, n$ and x_i represents the activity level of node i. The term $W_{i,j}$ is the directed connection strength, b_i is the external drive, and $[y]_+ = \max\{y, 0\}$ is the threshold nonlinearity. We consider competitive TLNs, which are the case $W_{i,j} \leq 0,\ W_{i,i} = 0$, and $b_i \geq 1$. Furthermore, we consider the connection strength

$$W_{ij} = \begin{cases} 0 & \text{if } i = j, \\ -1 + \lambda & \text{if node } j \text{ is connected to node } i, \\ -1 - \delta & \text{else.} \end{cases}$$

This model has shown complex behavior, including quasiperiodicity [ref]. We replicate the quasiperiodic behavior of Figure 2 in [ref]. We refer to it for the initial condition and connection matrix. The rest of the parameter values are $n = 25,\ b_i = 1,\ \lambda = 0.25$, and $\delta = 0.5$.. We solve up to $t = 600$ and perform SW with $f = x_4,\ d = 4,\ \tau = 27.53$, and $\epsilon = 0.07$, see Figure 5.6.

5.2.7 Restricted Three Body Problem

In celestial mechanics, the restricted three body problem (RTBP) offers an accessible model with known equilibrium points [52]. The equations describe the progression of three celestial bodies in which one of them is considered a massless particle. The other two bodies, denotes as primaries, are assumed to move in circular orbits around their center of mass. By taking a coordinate system that rotates with the primaries and under the appropriate scaling, it can be assumed the primaries have masses $1 - \mu$ and μ, $\mu \in [0, 1/2]$, are fixed at $(\mu, 0, 0)$ and $(\mu - 1, 0, 0)$, respectively, and complete one revolution in 2π [41]. This framework allows us to express the motion of the massless particle by the equations

$$\ddot{x} - 2\dot{y} = \Omega_x,$$

$$\ddot{y} + 2\dot{x} = \Omega_y,$$

$$\ddot{z} = \Omega_z,$$

where

$$\Omega = \frac{1}{2}(x^2 + y^2) + \frac{1 - \mu}{r_1} + \frac{\mu}{r_2} + \frac{1}{2}\mu(1 - \mu),$$

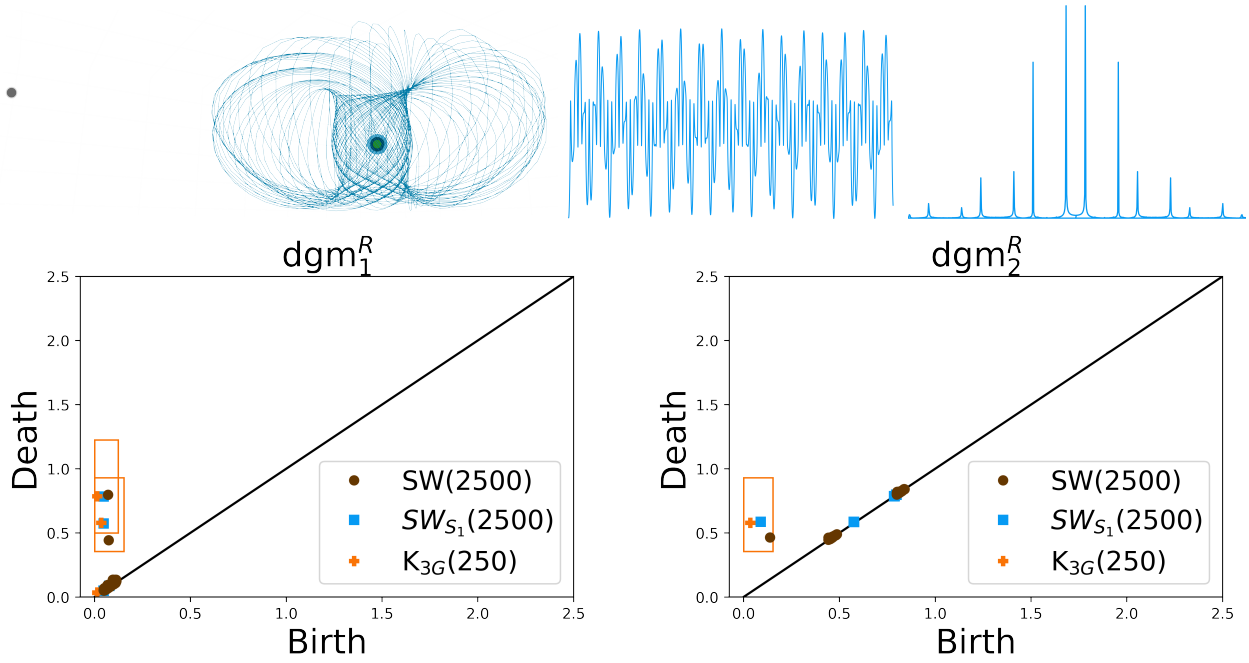

Figure 5.7 Top row: Phase space depiction of RTBP in (x, y, z) space. We include the Earth, shown in blue and green, and the Moon, shown in grey. The solution $x(t)$ we used for SW is plotted in the middle followed by its fast fourier transform. Bottom row: Persistence diagrams.

and

$$r_1 = \sqrt{(x-\mu)^2 + y^2 + z^2}, \qquad r_2 = \sqrt{(x-\mu+1)^2 + y^2 + z^2}$$

are the distances from the particles to the primaries. The case of the Earth-Moon system is of particular interest since it can aid in spacecraft missions interested in the Sun and the magnetosphere of the Earth [41]. Indeed, near the equilibrium points of the system, quasiperiodicity is present which translates to nice trajectories for a mission. We replicate this behavior for the Earth-Moon system, see Figure 5.7. In this case, $\mu = 0.0121506$. We solve the system with the initial condition $(x_0, y_0, z_0, \dot{x}, \dot{y}, \dot{z}) = (-0.5, 0, 0, 0, 0, 0.73)$ up to $t = 100$. SW was done with $f = x$, $d = 4$, $\tau = 4.37$ and $\epsilon = 0.03$.

5.2.8 Bicircular Restricted Four Body Problem

Considering the effects of the sun in the RTBP model gives rise to the bicircular restricted four body problem (BCR4BP). The model is of importance for exploiting the force from the sun in trajectory designs for lunar missions and has found applications for ballistic lunar transfers to the lunar region [53]. The new model uses the same coordinate axes as the RTBP and the same circular

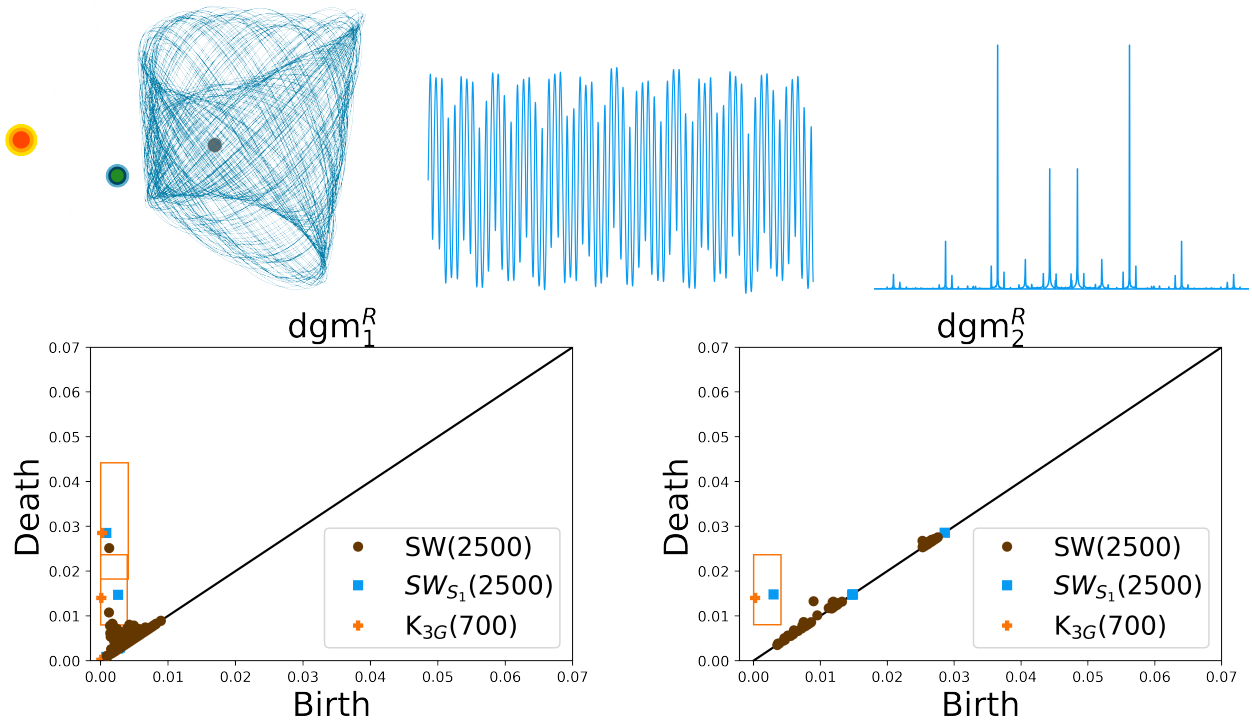

Figure 5.8 Top row: Phase space depiction of BCR4BP in (x, y, z) space. We include the Earth, shown in blue and green, the Moon, shown in grey, and the Sun, shown in red and yellow. We note the position of the Earth and Sun are not to scale. The solution $z(t)$ we used for SW is plotted in the middle followed by its fast fourier transform. Bottom row: Persistence diagrams.

motion assumptions of the Earth and Moon but it now includes terms pertaining to the influence of the Sun. The Sun is assumed to lie in the x-y plane at a fixed distance to the origin, a_4, and moving with a constant angular velocity, $\dot{\theta}_S$, in circular motion. Furthermore, the model assumes the Earth and Moon are not perturbed by solar gravity. Under these assumptions, the equations are [53]

$$\ddot{x} = 2\dot{y} + \frac{\partial \Upsilon}{\partial x},$$
$$\ddot{y} = -2\dot{x} + \frac{\partial \Upsilon}{\partial y},$$
$$\ddot{z} = \frac{\partial \Upsilon}{\partial z},$$

where

$$\Upsilon = \frac{1-\mu}{r_{13}} + \frac{\mu}{r_{23}} + \frac{x^2+y^2}{2} + \lambda\left(\frac{m_4}{r_{43}} - \frac{m_4}{a_4^3}(x_4 x + y_4 y + z_4 z)\right).$$

and (x_4, y_4, z_4) denotes the position of the sun, $r_{1,3}$, $r_{2,3}$, $r_{4,3}$ the distance of the Earth to the massless object, the Moon to the massless object, and the Sun to the massless object, respectively,

and m_4 is the non-dimensional mass of the Sun. We note the case $\lambda = 0$ reduced to the RTBP. A study of the system as λ increases to 1 is done in [53], where they showed the model exhibited quasiperiodicty. We replicate the quasiperiodic behavior, see Figure 5.8, for parameter values $\lambda = 1,\ \mu = 0.012155,\ a_4 = 388.84,\ m_4 = 328950.69$, and $\dot{\theta}_S = -0.9251986$. The system was solved with the initial condition $(x_0, y_0, z_0, \dot{x}, \dot{y}, \dot{z}, \theta_S) = (1.09, 0, 0, 0, 0.19, 0.05, 2)$ up to $t = 200$. SW was done with $f = z,\ d = 4,\ \tau = 39.99$ and $\epsilon = 0.009$.

5.3 Concluding Remarks

Table 5.1 Running Times

Example	SW	SW(S1)	K(3G)
5.2.1	7008.66 sec	7672.85 sec	0.87 sec
5.2.2	4351.15 sec	5351.15 sec	0.42 sec
5.2.3	3126.81 sec	3218.73 sec	0.50 sec
5.2.4	5556.86 sec	7628.48 sec	0.98 sec
5.2.5	5137.54 sec	6505.54 sec	0.66 sec
5.2.6	5805.28 sec	7193.97 sec	0.22 sec
5.2.7	6900.29 sec	7937.03 sec	2.09 sec
5.2.8	6615.33 sec	8231.25 sec	0.59 sec

In this section we detailed how 3G can be implemented on general quasiperiodic functions. Our approximation method was used on dynamical systems known to exhibit quasiperiodicity. As our figures show, we successfully approximated the diagrams obtained from SW. Error bounds can also be computed for our method. We illustrate them in the plots as rectangles. Furthermore, our approach significantly reduces computational time as shown in Table 5.1. We hope our work contributes to the implementation of the sliding window embedding technique on large data sets.

CHAPTER 6

CONTRIBUTION AND FUTURE WORK

We detailed how SW is a vital method used for the better understanding of quasiperiodic signals. The correspondence between a quasiperiodic function of N incommensurate frequencies and a N-dimensional torus make persistent homology an ideal component. However, the exponential computational cost of the latter limit the datasets that can be impacted by SW. Our contribution is providing an approximation to the persistence diagrams of interest (Section 1.1). Our method 3G achieves this within known error bounds. Our computation, on average, took less than 1 second to run for the examples depicted in Chapter 5. This contrast to an average computation time of 5,563 seconds when using a standard library, Ripser [16], to compute the persistence diagrams of interest (Table 5.1).

Future work for our project would be to improve our approximation by tightening the error bounds. A more granular approach would be to inspect the specific transformation matrix instead of relying on a singular value argument. Another direction is to apply our work to real world data such as electrocardiogram dataset.

BIBLIOGRAPHY

[1] H. R. Wilson and J. D. Cowan, "Excitatory and inhibitory interactions in localized populations of model neurons," *Biophysical journal*, vol. 12, no. 1, pp. 1–24, 1972.

[2] J. A. Perea, "Topological time series analysis," *Notices of the American Mathematical Society*, vol. 66, no. 5, pp. 686–694, 2019.

[3] F. Takens, "Detecting strange attractors in turbulence," in *Dynamical systems and turbulence, Warwick 1980*, pp. 366–381, Springer, 1981.

[4] P. Skraba, V. De Silva, and M. Vejdemo-Johansson, "Topological analysis of recurrent systems," in *NIPS 2012 Workshop on Algebraic Topology and Machine Learning, December 8th, Lake Tahoe, Nevada*, pp. 1–5, 2012.

[5] H. Gakhar and J. A. Perea, "Sliding window persistence of quasiperiodic functions," *arXiv preprint arXiv:2103.04540*, 2021.

[6] C. J. Tralie and J. A. Perea, "(quasi) periodicity quantification in video data, using topology," *SIAM Journal on Imaging Sciences*, vol. 11, no. 2, pp. 1049–1077, 2018.

[7] J. A. Perea, A. Deckard, S. B. Haase, and J. Harer, "Sw1pers: Sliding windows and 1-persistence scoring; discovering periodicity in gene expression time series data," *BMC bioinformatics*, vol. 16, no. 1, pp. 1–12, 2015.

[8] D. Levine and P. J. Steinhardt, "Quasicrystals: a new class of ordered structures," *Physical review letters*, vol. 53, no. 26, p. 2477, 1984.

[9] I. Wilden, H. Herzel, G. Peters, and G. Tembrock, "Subharmonics, biphonation, and deterministic chaos in mammal vocalization," *Bioacoustics*, vol. 9, no. 3, pp. 171–196, 1998.

[10] M. Belloy, M. Naeyaert, G. Keliris, A. Abbas, S. Keilholz, A. Van Der Linden, and M. Verhoye, "Dynamic resting state fmri in mice: detection of quasi-periodic patterns," *Proceeding of the International Soc. Magn. Reson. Med*, vol. 961, 2017.

[11] S. Noorzadeh, M. Niknazar, B. Rivet, J. Fontecave-Jallon, P.-Y. Guméry, and C. Jutten, "Modeling quasi-periodic signals by a non-parametric model: Application on fetal ecg extraction," in *2014 36th Annual International Conference of the IEEE Engineering in Medicine and Biology Society*, pp. 1889–1892, IEEE, 2014.

[12] D. Weixing, H. Wei, W. Xiaodong, and C. Yu, "Quasiperiodic transition to chaos in a plasma," *Physical review letters*, vol. 70, no. 2, p. 170, 1993.

[13] M. A. Quiroz-Juárez, R. Vázquez-Medina, E. Ryzhii, M. Ryzhii, and J. L. Aragón, "Quasiperiodicity route to chaos in cardiac conduction model," *Communications in Nonlinear Science*

and Numerical Simulation, vol. 42, pp. 370–378, 2017.

[14] H. Gakhar and J. A. Perea, "Künneth formulae in persistent homology," *arXiv preprint arXiv:1910.05656*, 2019.

[15] J.-D. Boissonnat, T. K. Dey, and C. Maria, "A space and time efficient implementation for computing persistent homology," tech. rep., INRIA Research Report 8195, 2012.

[16] U. Bauer, *Ripser*, vol. 514. URL: https://github. com/Ripser/ripser, 2016.

[17] N. O. Malott, S. Chen, and P. A. Wilsey, "A survey on the high-performance computation of persistent homology," *IEEE Transactions on Knowledge and Data Engineering*, vol. 35, no. 5, pp. 4466–4484, 2022.

[18] C. Olds, "Continued fractions," *Mathematical Association of America*, 1963.

[19] H. Hancock, "Development of the minkowski geometry of numbers," *(No Title)*, 1939.

[20] T. Van Ravenstein, "The three gap theorem (steinhaus conjecture)," *Journal of the Australian Mathematical Society*, vol. 45, no. 3, pp. 360–370, 1988.

[21] M. M. Murudi and S. M. Mane, "Seismic effectiveness of tuned mass damper (tmd) for different ground motion parameters," in *13th World Conference on Earthquake Engineering*, vol. 2, pp. 1–8, 2004.

[22] R. Wen, T. Li, and B. Zhen, "Quasi-periodic motions of a pendulum with vibrating suspension point," *Journal of Vibration Engineering & Technologies*, vol. 7, pp. 519–532, 2019.

[23] Phys.org, "Japanese companies look to quake damping pendulums," August 2013. Accessed: 2024-03-20.

[24] A. Hatcher, *Algebraic topology*. Cambridge: Cambridge University Press, 2002.

[25] E. J. Hanson and J. D. Rock, "Decomposition of pointwise finite-dimensional sˆ 1 persistence modules," *arXiv preprint arXiv:2006.13793*, 2020.

[26] Y. Cao, A. Monod, A. Vlontzos, L. Schmidtke, and B. Kainz, "Topological information retrieval with dilation-invariant bottleneck comparative measures," *Information and Inference: A Journal of the IMA*, vol. 12, no. 3, pp. 1964–1996, 2023.

[27] J. D. Cowan, J. Neuman, and W. van Drongelen, "Wilson–cowan equations for neocortical dynamics," *The Journal of Mathematical Neuroscience*, vol. 6, no. 1, pp. 1–24, 2016.

[28] G. F. Poggio and L. J. Viernstein, "Time series analysis of impulse sequences of thalamic somatic sensory neurons," *Journal of Neurophysiology*, vol. 27, no. 4, pp. 517–545, 1964.

[29] E. Robert, "Fourier series: a modern introduction," *Springer Science & Business Media*, vol. 2, 2012.

[30] C. F. Gauss, *Demonstratio nova theorematis omnem functionem algebraicam*. apvd CG Fleckeisen, 1799.

[31] A. Zhigljavsky and I. Aliev, "Kronecker sequences: Asymptotic distributions of the partition lengths,"

[32] N. Leong, *Sums of Reciprocals and the Three Distance Theorem*. PhD thesis, University of York, 2017.

[33] L. S. Salas and J. A. Perea, "Estimation of persistence diagrams via the three gap theorem." Manuscript under review, 2023.

[34] G. Lochs, "Vergleich der genauigkeit von dezimalbruch und kettenbruch," in *Abhandlungen aus dem Mathematischen Seminar der Universität Hamburg*, vol. 27, pp. 142–144, Springer, 1964.

[35] C. Faivre, "On decimal and continued fraction expansions of a real number," *Acta Arithmetica*, vol. 82, no. 2, pp. 119–128, 1997.

[36] N. Saul and C. Tralie, "Persim," 2019.

[37] D. Cohen-Steiner, H. Edelsbrunner, and J. Harer, "Stability of persistence diagrams," in *Proceedings of the twenty-first annual symposium on Computational geometry*, pp. 263–271, 2005.

[38] F. Chazal, V. De Silva, M. Glisse, and S. Oudot, *The structure and stability of persistence modules*, vol. 10. Springer, 2016.

[39] T. Detroux, G. Habib, L. Masset, and G. Kerschen, "Performance, robustness and sensitivity analysis of the nonlinear tuned vibration absorber," *Mechanical Systems and Signal Processing*, vol. 60, pp. 799–809, 2015.

[40] E. Kaslik, E.-A. Kokovics, and A. Rădulescu, "Stability and bifurcations in wilson-cowan systems with distributed delays, and an application to basal ganglia interactions," *Communications in Nonlinear Science and Numerical Simulation*, vol. 104, p. 105984, 2022.

[41] G. Gómez and J. M. Mondelo, "The dynamics around the collinear equilibrium points of the rtbp," *Physica D: Nonlinear Phenomena*, vol. 157, no. 4, pp. 283–321, 2001.

[42] C. E. Shannon, "Communication in the presence of noise," *Proceedings of the IRE*, vol. 37, no. 1, pp. 10–21, 1949.

[43] S. C. Shadden, F. Lekien, and J. E. Marsden, "Definition and properties of lagrangian coherent structures from finite-time lyapunov exponents in two-dimensional aperiodic flows," *Physica D: Nonlinear Phenomena*, vol. 212, no. 3-4, pp. 271–304, 2005.

[44] G. D. Charó, G. Artana, and D. Sciamarella, "Topology of dynamical reconstructions from lagrangian data," *Physica D: Nonlinear Phenomena*, vol. 405, p. 132371, 2020.

[45] J. Penalva Vadell, "Takens' theorem: Proof and applications," 2018.

[46] S. Coombes and C. Laing, "Delays in activity-based neural networks," *Philosophical Transactions of the Royal Society A: Mathematical, Physical and Engineering Sciences*, vol. 367, no. 1891, pp. 1117–1129, 2009.

[47] A. J. N. Holgado, J. R. Terry, and R. Bogacz, "Conditions for the generation of beta oscillations in the subthalamic nucleus–globus pallidus network," *Journal of Neuroscience*, vol. 30, no. 37, pp. 12340–12352, 2010.

[48] H. R. Wilson, "Simplified dynamics of human and mammalian neocortical neurons," *Journal of theoretical biology*, vol. 200, no. 4, pp. 375–388, 1999.

[49] Z. Ju, Y. Lin, B. Chen, H. Wu, M. Chen, and Q. Xu, "Electromagnetic radiation induced non-chaotic behaviors in a wilson neuron model," *Chinese Journal of Physics*, vol. 77, pp. 214–222, 2022.

[50] Q. Xu, Z. Ju, C. Feng, H. Wu, and M. Chen, "Analogy circuit synthesis and dynamics confirmation of a bipolar pulse current-forced 2d wilson neuron model," *The European Physical Journal Special Topics*, vol. 230, no. 7, pp. 1989–1997, 2021.

[51] B. Bao, H. Qian, Q. Xu, M. Chen, J. Wang, and Y. Yu, "Coexisting behaviors of asymmetric attractors in hyperbolic-type memristor based hopfield neural network," *Frontiers in Computational Neuroscience*, vol. 11, p. 81, 2017.

[52] W. S. Koon, M. W. Lo, J. E. Marsden, and S. D. Ross, "Heteroclinic connections between periodic orbits and resonance transitions in celestial mechanics," *Chaos: An Interdisciplinary Journal of Nonlinear Science*, vol. 10, no. 2, pp. 427–469, 2000.

[53] B. P. McCarthy and K. C. Howell, "Four-body cislunar quasi-periodic orbits and their application to ballistic lunar transfer design," *Advances in Space Research*, vol. 71, no. 1, pp. 556–584, 2023.